Flow (2025), **5** E35
doi:10.1017/flo.2025.10026

FLOW CAMBRIDGE UNIVERSITY PRESS

RESEARCH ARTICLE

Tip leakage flow structure and cavitation inception in a ducted marine propeller

Ayush Saraswat, Chintan Panigrahi, Kirtivardhan Singh and Joseph Katz

Department of Mechanical Engineering, Johns Hopkins University, Baltimore, MD, USA
Corresponding author: Joseph Katz; Email: katz@jhu.edu

Received: 1 March 2025; **Revised:** 16 August 2025; **Accepted:** 20 August 2025

Keywords: marine propeller; cavitation inception; particle image velocimetry; tip leakage flow; tip leakage vortex

Abstract

Cavitation inception and the associated flow structure in the tip region of a ducted propeller are investigated experimentally at varying advance ratios (J) using high-speed imaging and stereoscopic particle image velocimetry (SPIV) measurements in a refractive index-matched facility. At design and higher J values, inception occurs in axially aligned secondary vortices, located between the blade suction side and the tip leakage vortex (TLV), circumferentially after the trailing edge. With decreasing J, the inception shifts first to the TLV, and then along its core towards the leading edge. High-resolution SPIV data follow the evolution of TLV, tip leakage flow, near wake and several secondary vortices. Time-resolved SPIV at 30 kHz enables calculation of all three mean vorticity components, hence capturing axial vortices, and identifies the origin of flow structures. At high J values, inception occurs when quasi-axial vortices are stretched by the circumferential TLV and co-rotating secondary vortices located in the shear layer connecting the TLV to the suction side blade tip. With decreasing J, inception shifts to the TLV and towards the leading edge owing to earlier rollup and higher vortex strength, along with earlier breakup, evidenced by high core turbulence and a decrease in peak vorticity despite an increase in circulation.

Impact Statement

Cavitation on marine propellers has several adverse effects, including performance degradation, erosion and noise. Hence, prediction of conditions, location and mechanisms of cavitation inception is a crucial part of the propeller design process. While past studies have shown that cavitation inception in ducted propellers occurs in secondary vortices associated with tip leakage flows, the origin and mechanism involved are unclear. Using a unique refractive index-matched facility, high-resolution and time-resolved stereoscopic particle image velocimetry and high-speed imaging, this study investigates how interacting vortices developing around the blade tip affect cavitation inception in an acrylic ducted propeller. At design conditions, cavitation inception occurs within axial vortices originating from the blade suction side near the trailing edge. The pressure minima in these vortices are caused by axial straining induced by multiple circumferential vortices, including the tip leakage vortex (TLV) and secondary structures, residing in the shear layer separating the leakage and passage flows. With decreasing advance ratio, the TLV increases in strength, and the inception site shifts to its core. The detailed measurements provide a comprehensive view of the underlying phenomena, including, e.g., the origin of vortical structures, facilitating improved design and modelling.

1. Introduction

In vortex-dominated flows, cavitation inception frequently occurs along the core of vortices owing to low pressure there (Arndt, 2002). Tip vortices developing around fixed hydrofoils and wings are areas in which this phenomenon has been studied extensively, both for open configuration, where the tip is

located far from boundaries (e.g., Higuchi *et al.,* 1989; Fruman and Aflalo, 1989; Arndt *et al.,* 1991; Stinebring *et al.,* 1991; Ganesh *et al.,* 2014; Brandao *et al.,* 2024) or for cases with a narrow gap between the tip and an endwall (e.g., Boulon *et al.,* 1999; Gopalan *et al.,* 2002; Russell *et al.,* 2023). Other flows that involve multiple vortices include turbulent shear layers and separated flows (Katz, 1984; Katz and O'Hern, 1986; Agarwal *et al.,* 2023), jets (Ooi, 1985; Ran and Katz, 1994; Gopalan *et al.,* 1999), wakes (Wu *et al.,* 2021) and targeted studies focusing on interactions among vortex pairs (Choi *et al.,* 2003; Chang *et al.,* 2007, 2012). In several of these cases, stretching of smaller secondary vortices by larger ones increases their core vorticity, hence reducing their core pressure, and cavitation inception preferentially occurs in the weaker secondary structures. Flow physics becomes more complex in rotating turbomachines, such as pumps and propellers, owing to the effects of rotation, blade interactions and large velocity gradients between the blade tip and the stationary endwall in the cases of ducted machines (Farrell and Billet, 1994; Gindroz and Billet, 1998). While the performance and cavitation characteristics in open propellers have been studied extensively (e.g., Sharma *et al.,* 1990; Felli and Falchi, 2011; Park *et al.,* 2014), the information about tip leakage flows and cavitation in their ducted counterparts is limited.

It is well established that encasing a marine propeller affects its tip flow structure and improves its thrust and efficiency (Thurston and Amsler, 1966; Thurston and Evanbar, 1968; Rajagopalan and Zhaoxing, 1989). The duct inherently alters the structure and distribution of vortices around the blade tip, hence the location and condition for cavitation inception. Chesnakas and Jessup (2003) have shown that cavitation inception in a ducted propeller near design conditions occurs circumferentially downstream of the blade trailing edge (TE), in a region where the tip leakage vortex (TLV) merges with a co-rotating vortex that appears to originate from the blade TE, hence they refer to it as 'trailing edge vortex'. Corresponding Reynolds-averaged Navier–Stokes (RANS) simulations by Kim *et al.* (2006) and localised direct numerical simulations by Hsiao and Chahine (2006, 2008) have shown that pressure minima indeed appear circumferentially behind the blade TE, but with differences in location and pressure magnitude. Velocity measurements using two-dimensional (2-D) particle image velocimetry (PIV) behind the same propeller by Oweis and Ceccio (2005) have shown that, in addition to the TLV, the flow consists of multiple counter- and co-rotating secondary vortices. The existence of such structures is characteristic of several ducted axial turbomachines, e.g., waterjet pumps (Wu *et al.,* 2011a), and aviation compressor rotors (Chen *et al.,* 2017). Subsequently, Oweis *et al.* (2006) compare the tip flow with and without a duct for the same propeller and conclude that the duct reduces the strength of the primary tip vortex relative to that of the secondary structures, and increases the variability in vortex size and position, as well as the velocity fluctuations. More recently, large eddy simulations, by Leasca *et al.* (2024), of the flow around the same propeller show that the low-pressure regions form as secondary vortices wrap around the primary TLV. However, they do not observe a persistent TE vortex. In another recent paper, Michael *et al.* (2024) introduce and test a new 901.8 mm diameter, two-bladed, ducted propeller (details follow), which they name P5757. In agreement with the previous studies, they experimentally observe that at design conditions, cavitation inception occurs circumferentially downstream of the blade TE, but axially upstream of it. Their improved delayed detached eddy simulations also show the existence of secondary vortices around the primary TLV in the vicinity of the cavitation inception area, but they do not identify a specific TE vortex or a particular structure causing the cavitation inception. Tests of a one-third replica of this propeller in our laboratory (Saraswat *et al.,* 2024) also show the same location for the onset of cavitation at design conditions, shifting to the core of the primary TLV at lower flow rates.

Obtaining detailed flow data within the rotating blade rows of a ducted turbomachine, especially in the tip gap, is a challenge because of the limited physical and optical access to this region. As a result, many of the flow measurement studies focus on the blade wake region (e.g. Chesnakas and Jessup, 2003; Oweis and Ceccio, 2005). Some studies have also utilised annular cascades with rotating hubs (Doukelis *et al.,* 1998), and linear cascades with moving walls (Wang and Devenport, 2004) to study the effect of tip leakage flow in simpler configurations. As discussed later, we have addressed the access problem by

performing the measurements in a refractive index-matched turbomachine facility, where the refractive index of the transparent acrylic blades and casing is matched with that of the liquid.

The measurements discussed in this paper have been performed around the abovementioned 300.6 mm diameter replica of the two-bladed P5757 propeller. Our objective is to characterise the location of cavitation inception and the evolution of the flow structure around the propeller blade tip region under varying operating conditions. The spatial extent of the flow measurement domain encompasses the duct boundary layer upstream of the propeller, the entire blade tip, including the areas of TLV rollup and its interaction with entrained secondary structures, as well as the near wake circumferentially downstream of the blade. The data consist of results of high-speed (10–25 kHz) imaging of incipient and developed cavitation, as well as stereoscopic particle image velocimetry (SPIV) measurements in the non-cavitating flows. The latter includes two separate datasets, the first having higher-resolution but phase-locked data, and the second is time resolved (30 kHz) but has a lower resolution. Data have been acquired at design, near-design, as well as far below design conditions. The high-resolution SPIV dataset is used for characterising the evolution of mean flow and turbulent kinetic energy (TKE), and the high-speed dataset allows reconstruction of the entire 3-D mean vorticity field, focusing specifically on the cavitation inception region. Comparisons of the cavitation visualisations and the SPIV results elucidate the physical mechanisms governing the onset of cavitation.

While most of the present discussions focus on conditions extending from 5% below to 10% above the design point, sample results highlighting specific similarities and differences are also presented for lower off-design conditions. Particular attention is paid to the origin of secondary structures and their interaction with the TLV near the propeller TE. For example, some of the secondary structures originate from the entrainment of the suction side (SS) boundary layers, while others originate from the pressure side (PS) and are entrained into the tip gap. The role of the counter-rotating vortices initiated by the entrainment of the endwall boundary layer is also discussed. Statistics of flow mechanisms associated with cavitation inception and examples of instantaneous flow are presented to highlight features that are 'smeared' by ensemble averaging. We also present data on the effect of operating conditions on the evolution of the tip leakage flow, and strength and trajectory of the TLV and secondary vortices. While not a primary focus, we also include the distributions of TKE and discuss the impact of changing operating conditions on turbulence. The outline of the paper is as follows: the facility, propeller geometry, measurement set-ups and details of the techniques are described in the next section. The results are shown next, followed by a discussion and conclusions.

2. Experimental facility and measurement techniques

The JHU refractive index-matched turbomachine facility is a horizontal, variable pressure and flow rate tunnel that has been in use since the early 2000s to study ducted axial turbomachines. It utilises an aqueous solution of sodium iodide as the working fluid that has a specific gravity of 1.83 and a kinematic viscosity of $\nu = 1.1 \times 10^{-6}$ m^2 s^{-1}. The salt concentration is adjusted to match its refractive index to that of acrylic (Bai and Katz, 2014). The general dimensions, pressure, temperature and flow rate controls of the facility are described in Wu *et al.* (2011a) and Chen *et al.* (2017). A couple of sketches illustrating an isometric and a sectional view of the test section assembly are shown in figure 1(*a*, *b*), respectively. A new transparent housing, with flat external walls and a 304.8 mm diameter, constant area, circular duct as the internal wall, has been constructed to host the present two-bladed propeller. The flat surfaces facilitate the attachment of viewing prisms and PIV instrumentation. The propeller is driven by a shaft connected to an external 60 HP motor (not shown). This shaft is located inside a non-rotating sleeve, a streamlined transition cone up to the test section, and stationary spacers upstream and downstream of the propeller. The only rotating parts exposed to the flow are the propeller hub and the blades. The shaft is supported by ball bearings at both the upstream and downstream ends of the test section. An additional bearing is located at the transition between the spacer and the hub upstream of the propeller. The upstream bearings are housed in a stainless-steel honeycomb of depth 22 mm and cell size 3 mm.

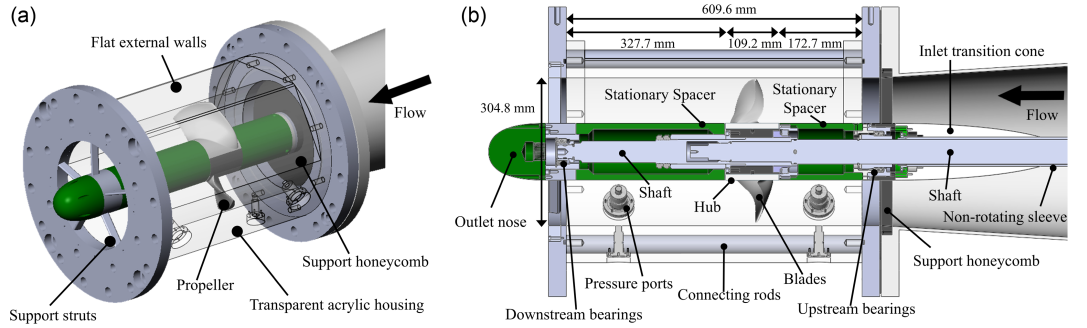

Figure 1. *Schematic of the ducted propeller test section assembly: (a) isometric view of the assembly (connecting rods not shown), (b) sectional view of the assembly.*

Two additional honeycombs with central bronze bushings to support the shaft (not shown) are located upstream of the shown area. Together, they serve as flow straighteners, providing a uniform flow with negligible swirl upstream of the propeller (shown later). The downstream bearings are installed within a cylindrical housing supported by five streamlined struts. The test section also has two pairs of wall static pressure ports located upstream and downstream of the propeller for characterising the pressure rise and inlet pressure to the propeller. Two additional ports are available for further instrumentation or drainage.

To control the flow rate, the return line of the facility has a secondary propeller driven by a 20 HP motor whose speed can be adjusted independently, and a variable resistance valve consisting of perforated disks that can be rotated relative to each other. The latter has been kept completely open during the current experiments. The flow rate is calculated by interpolating and integrating the axial velocity profile measured in the return line by radially traversing a pitot tube, connected to a Setra Model 230 differential pressure transducer, along four diametrical paths aligned circumferentially at 45° to each other. Once calibrated, the operating condition is fixed and monitored based on the static-to-static pressure rise across the propeller at a given motor speed using another differential transducer of the same model. Both transducers are calibrated using a mercury manometer before each test. The estimated uncertainty in the flow rate and pressure rise is 1.7% and 1.2%, respectively (Chen *et al.,* 2017). The mean pressure at the inlet to the pump, which is measured using a third transducer, is controlled by connecting a partially filled overhead tank either to a vacuum pump or to a source of compressed nitrogen gas. As part of performance measurements, the total torque of the propeller is measured using an inline (shaft-driven) strain gauge-based torque meter (SensorData® T261-STD-A), which has a manufacturer-specified uncertainty of 0.1%. The sensor is integrated with the shaft before it enters the facility. The base torque required to overcome the mechanical resistance of the bearing assemblies is first measured by running the motor at the same speeds, with the blades removed, and the hub slots filled to create a complete cylinder. The hydrodynamic torque (Q) is obtained by subtracting the base torque from the total torque.

The geometric details of Propeller P5757 are provided in Michael *et al.* (2024). It is a preferentially tip-loaded propeller with tip edges rounded to prevent any attached surface cavitation before tip leakage cavitation. For our scaled replica, the chords at the hub and the tip are 150 mm, and the corresponding axial chords are 82 mm and 41 mm. The endwall and hub diameters are 304.8 mm and 117 mm, respectively, and the through-flow area is 62215 mm^2. The resulting tip diameter and nominal tip gap are 300.6 and 2.1 mm, respectively. However, due to manufacturing tolerances for both blades and the duct, the measured tip gap, using precision gauge pins, is 1.9 ± 0.02 mm throughout the blade tip and duct circumference. The blades and part of its base are machined out of acrylic blocks and then bolted to a black-anodised aluminium hub. The axial gaps between the rotating hub and the stationary spacers on both sides are 1 mm. There is no path for the flow to leak across the propeller hub. The operating

Table 1. *Experimental operating conditions and kinematic parameters*

J	V_z (ms^{-1})	RPM	U_T (ms^{-1})	$Re_{tip}=U_Tc/\nu$	u_τ	Re_τ
0.68	1.95	572	9.0	1.23×10^6	–	–
0.803	2.30	572	9.0	1.23×10^6	0.087	2757
0.85	2.30	540	8.5	1.16×10^6	0.088	2459
0.933	2.30	492	7.7	1.05×10^6	0.089	2298

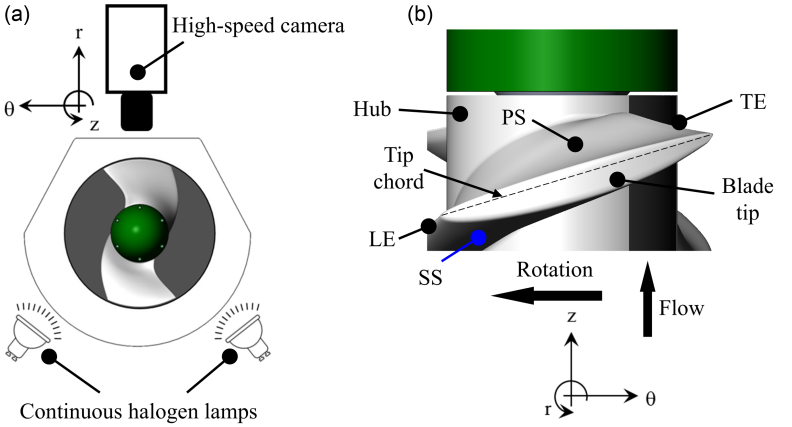

Figure 2. *Experimental set-up for visualisation of tip leakage cavitation: (a) view from the downstream end, (b) blade orientation in the cavitation images.*

condition of the propeller is characterised in terms of its advance ratio, $J=V_z/nD$, where V_z is the spatially averaged axial velocity obtained by dividing the flow rate by the through-flow area of the duct, n is the rotor speed in r.p.s. and D is the nominal propeller tip diameter. The present study provides data for the series of advance ratios tabulated in table 1, including the design advance ratio of this machine, $J = 0.85$ (Michael *et al.,* 2024). The corresponding blade tip speed U_T, and the blade tip Reynolds number Re_{tip} are also shown. We refer to $J = 0.803$, 0.85, 0.933 as the 'near-design' conditions. For these cases, V_z is constant, and J is varied by changing the propeller RPM. The lowest advance ratio case of $J = 0.68$, which is referred to as the 'off-design' condition, is attained by fixing the propeller RPM to that of $J = 0.803$ and varying the V_z.

The set-up used for visualisation of tip leakage cavitation and detection of cavitation inception is shown in figure 2(*a*). Both involve the use of a Phantom v2640 high-speed CMOS camera to acquire 1024×976 pixels images of the propeller tip region at a rate of 10 kHz to detect incipient cavitation, and at 25 kHz to visualise developed cavitation. Four continuous halogen lamps placed underneath the transparent test section are used for illumination. The orientation of the blade in the images is illustrated in figure 2(*b*). To remove the visible nuclei from the facility, it is kept under low pressure for a prolonged period while the liquid is degassed by deliberately cavitating the secondary propeller. The larger/visible nuclei are collected using multiple vertical pipes that are located in the return line and lead to an overhead tank connected to the facility. All the cavitation inception tests are performed at a total dissolved gas content of 80% saturation at atmospheric pressure, as measured by an InWater Technologies®, membrane-based, total dissolved gas probe. Before the tests, the pressure is increased and maintained at about 2-3 atm for at least 10-15 minutes, while observing the bubble population at the top of the test section. This process results in the disappearance of essentially all the visible bubbles, reducing the characteristic nuclei sizes to sub-visual levels (~27 μm/pixel). At the onset of data acquisition, the pressure is reduced within a few seconds, while acquiring high-speed images and synchronously recording the output of the pressure transducer connected to the inlet to the propeller, until

Table 2. *The SPIV parameters*

Parameter	Phase-locked SPIV	High-speed SPIV
Frame rate	2-4 f.p.s.	30000 f.p.s.
Interframe time	20 μs	33.33 μs
Camera pixel size	5.5 μm	27 μm (binning mode)
Camera resolution	6600 × 4400 pixels (~29 MP)	1024 × 512 pixels (~0.5 MP)
Magnification	94.6 pixels mm^{-1}	24.9 pixels mm^{-1}
Final interrogation window	32 × 32 pixels (50% overlap)	12 × 12 pixels (50% overlap)
Vector resolution	0.17 mm	0.24 mm
Realisations for ensemble averaging	2300–2400	104–120
Number of planes visualised	9	1574–1830

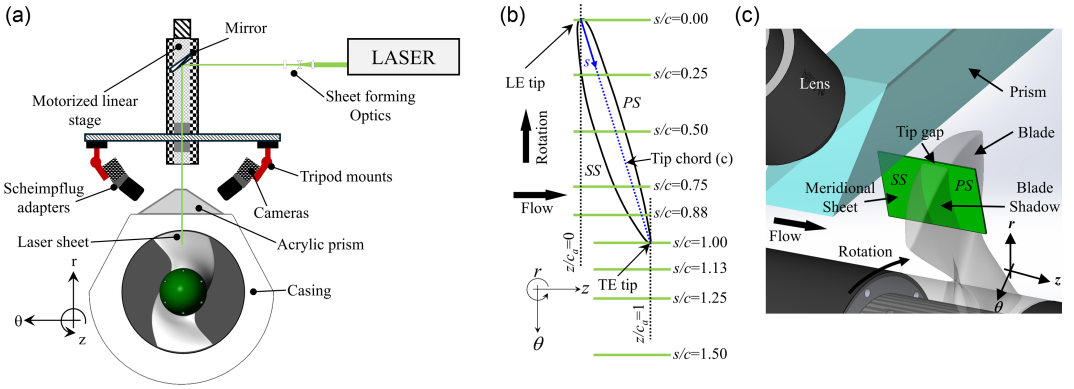

Figure 3. *(a) Experimental set-up for SPIV. (b) Locations of the meridional planes for phase-locked SPIV relative to the blade. (c) Illustration of the meridional FOV showing the intersection of laser sheet with the blade.*

cavitation appears. For visualisation of developed cavitation, the facility is operated at a constant mean pressure while acquiring data.

The SPIV set-up is illustrated in figure 3(*a*). During these measurements, the cavitation is suppressed completely by increasing the mean pressure of the facility to a sufficiently high level. For the phase-locked dataset, we use a pair of 6600 × 4400 pixels, Imperx B6640 CCD cameras, each equipped with a 105 mm lens and a Scheimpflug adapter. Illumination is provided by a 1 mm-thick sheet from a Quantel Evergreen 200 dual-head Nd:YAG laser. For the high-speed SPIV dataset, we use a pair of Phantom v2640 cameras equipped with the same lenses and adapters, and a Photonics DMX100-532DH Nd:YAG laser generating the light sheet. Key parameters of both datasets are compared in table 2. Data are acquired in meridional (*r*-*z*) planes for several blade orientations, defined in terms of s/c, where s is the chordwise coordinate and c is the blade tip chord (figure 3(*b*)). The blade tip leading edge (LE) is located at $s/c = 0$, and the tip TE is at $s/c = 1$. The phase-locked data are recorded at nine orientations spanning $s/c = 0$ to 1.50, as indicated in figure 3(*b*). The axial extent of the field of view (FOV) is $-0.1 \leq z/c_a \leq 1$, where c_a is the axial chord, for planes intersecting with the blade ($s/c < 1.0$). To cover the vortical structures circumferentially after the blade, the FOV is shifted axially downstream to $0.2 \leq z/c_a \leq 1.3$. For the high-speed SPIV, the axial extent is $0.35 \leq z/c_a \leq 1.3$, and the dataset covers the full propeller circumference in steps of $s/c \sim 0.002$, i.e., the propeller displacement between exposures. The flow is seeded with silver-coated, 13 μm diameter hollow glass spheres that have a specific gravity of 1.6, i.e., slightly lower than that of the working fluid. The image calibration is performed in two steps. Coarse calibration involves recording images of a target inside a container having the same fluid outside the test facility by traversing the entire imaging system as a single unit. The fine calibration (Wieneke, 2005) is based on the SPIV images recorded inside the facility. The SPIV images are

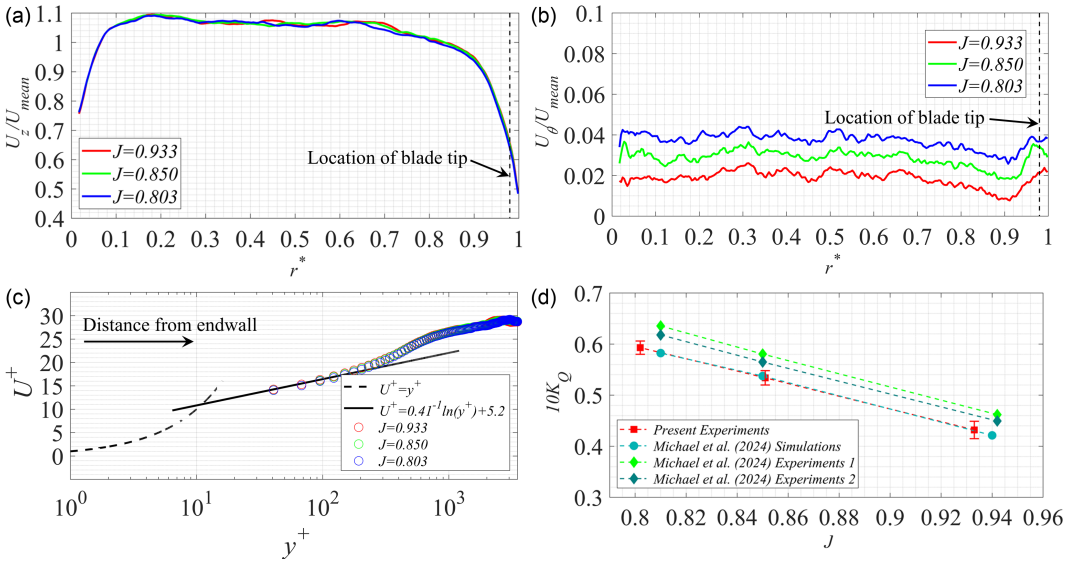

Figure 4. *(a, b) Mean axial and circumferential velocity profiles measured upstream of the propeller for the three near-design values of J. The location of the blade tip is marked with a dashed line. (c) Mean axial velocity profile in the upper 50% span, plotted on a semi-log scale. (d) Measured torque coefficient compared with experimental results and RANS simulations of Michael et al. (2024).*

pre-processed using background subtraction and contrast enhancement procedures, some available in-house (Roth and Katz, 2001), and others as part of the LaVision DaVis® commercial package. Vector calculations are performed using multi-pass cross-correlation available in the DaVis® 10.2 software, with the final interrogation window sizes indicated in table 2. For the phase-locked data, ensemble-averaged flow quantities are based on at least 2300 realisations. For the high-speed data, recorded in 1574–1830 planes depending on the rotor speed, averaging in each plane is based on 104–120 realisations. The planes are separated by an angular gap of 2×10^{-3} radians, corresponding to circumferential distances of 0.305 mm at the duct and 0.267 mm at $r^* = 0.8$, the bottom of the shown FOV. Since these values are of a similar order of magnitude as the in-plane vector spacing, 0.24 mm, we use the high-speed SPIV data for calculating all three components of the ensemble-averaged vorticity. Second-order finite differencing is used for determining both the in-plane and out-of-plane velocity gradients. The estimated uncertainty in instantaneous velocity is 2%, assuming that at least 3–5 particles are present in most of the interrogation windows and that their displacements are within 25%–50% of the final window size. On averaging over $n_s = 2300$ realisations, the uncertainty due to random errors is reduced by an order of magnitude to approximately 0.2%, assuming the scaling as $\sim 1/\sqrt{n_s}$. The associated uncertainty in turbulence quantities is expected to be an order of magnitude higher (Benedict and Gould, 1996), not accounting for the effects of finite spatial resolution.

In addition to the above datasets, for the $J = 0.803$, 0.85, 0.933 cases, we have also characterised the inflow velocity profiles averaged over 500 instantaneous realisations, using SPIV in a meridional plane and phase-locked to the blade LE. The set-up used is the same as shown in figure 3(*a*), but with a 60 mm lens. The resulting vector spacing is 0.34 mm. The axial and circumferential velocity profiles at $z = -2.8c_a$ or $-0.77c$ are plotted in figure 4(*a*, *b*), respectively. Here, and for the rest of this paper, the radial coordinate is expressed in terms of $r^* = (r - r_h)/(r_c - r_h)$, where the subscripts h and c refer to the blade hub and casing, respectively, i.e., r^* varies between 0 and 1. The values are normalised using U_{mean}, the radially averaged axial velocity. The magnitude of U_{mean}, 2.4 ms^{-1}, is 4.3% higher than the corresponding value of V_z, 2.3 ms^{-1}, presumably owing to circumferential variations and proximity to the blade. Due to laser reflections from the non-transparent upstream spacer, the measurements do not extend to the hub. The location of the blade tip, marked with a dashed line, indicates that the tip

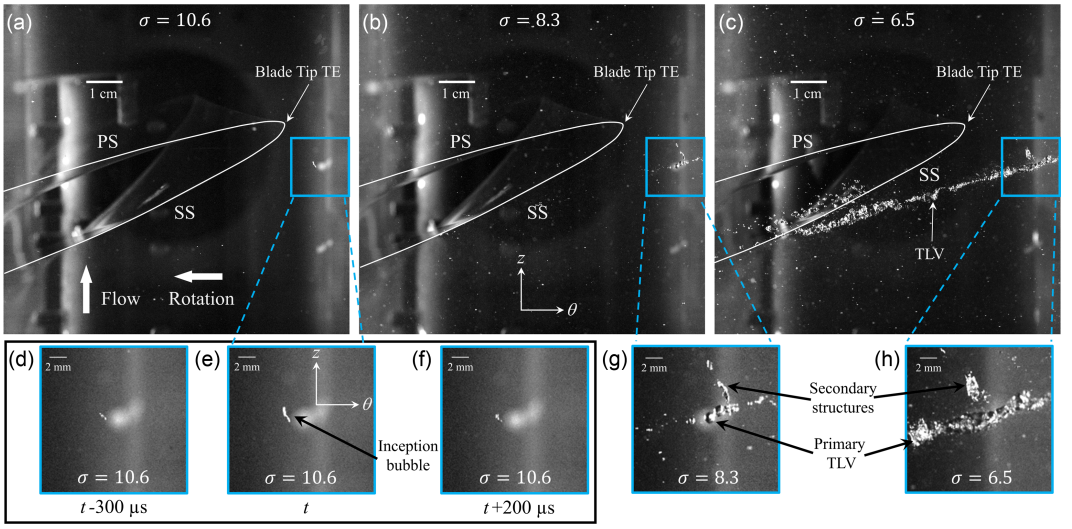

Figure 5. *Sample examples of cavitation for J = 0.85: (a) σ = 10.6, (b) σ = 8.3, (c) σ = 6.5. Corresponding magnified views of the regions highlighted by blue boxes are shown in the bottom row: (d–f) time evolution of the inception bubble at σ = 10.6, (g) magnified view at σ = 8.3, (h) magnified view at σ = 6.5.*

is located within the casing boundary layer. For the three cases shown here, the differences in axial velocity are very small. The circumferential velocity increases from 2% to 4% of U_{mean} with increasing J, suggesting that the trend is caused by the proximity to the blade LE. The radial variations in each profile fall within $\pm 0.005 U_{mean}$, except near the endwall casing, where each profile has a $0.01 U_{mean}$ dip at $r^* = 0.9$, and increases again near the endwall. The mean velocity profiles in the outer 50% of the span, starting from the endwall, are plotted on a semi-log scale in figure 4(*c*). The present SPIV resolution is insufficient for resolving the inner part of the turbulent boundary layers, so their profile begins in the log region. The endwall friction velocities (u_τ), also tabulated in table 1, are estimated by a fit to the velocity profiles at $30 < y^+ < 200$, with $y = 0$ being located at the duct endwall, and $y^+ = y u_\tau / \upsilon$. Estimates of the boundary layer thickness (δ) based on 99% of free-stream velocity are subjective due to small non-uniformities in the profile (figure 4(*a*)). Hence, it is estimated as the point where the outer wake region profile ($y^+ > 1000$) first flattens in figure 4(*c*). The values of u_τ and the endwall friction Reynolds number, $Re_\tau = \delta u_\tau / \nu$, are also provided in table 1. Consistent with Michael *et al.* (2024), Re_τ increases as the propeller RPM increases and as J decreases. Figure 4(*d*) compares the measured torque coefficients of the propeller, $10K_Q = 10Q/\rho n^2 D^5$, with the results of RANS simulations and experiments reported by Michael *et al.* (2024). The present experimental values are shown with their 95% confidence interval and agree with the magnitudes and trends of the simulations.

3. Results and discussion

3.1. Tip leakage cavitation

In this section, we discuss the location of cavitation inception, the magnitude of cavitation inception indices, and the evolution of cavitation with decreasing pressure as a function of advance ratio. Sample images of cavitation in the tip region for different cavitation indices (σ), all at design J (=0.85), are shown in figure 5. Here, $\sigma = (p_{in} - p_v)/0.5\rho V_z^2$, where p_{in} is the centre line pressure at the inlet to the test section, p_v is the vapour pressure of the NaI solution at 20-25°C (=1.2 *kPa*, Patil *et al.,* 1991) and $V_z = 2.3$ ms^{-1}. A white line is drawn along the blade tip to highlight its location, and the insets presented in the second row are enlarged views of the encased areas. As demonstrated by supplementary movie 1 and figure 5(*a*), at $J = 0.85$, cavitation inception typically appears as almost axially aligned, 1-2 mm

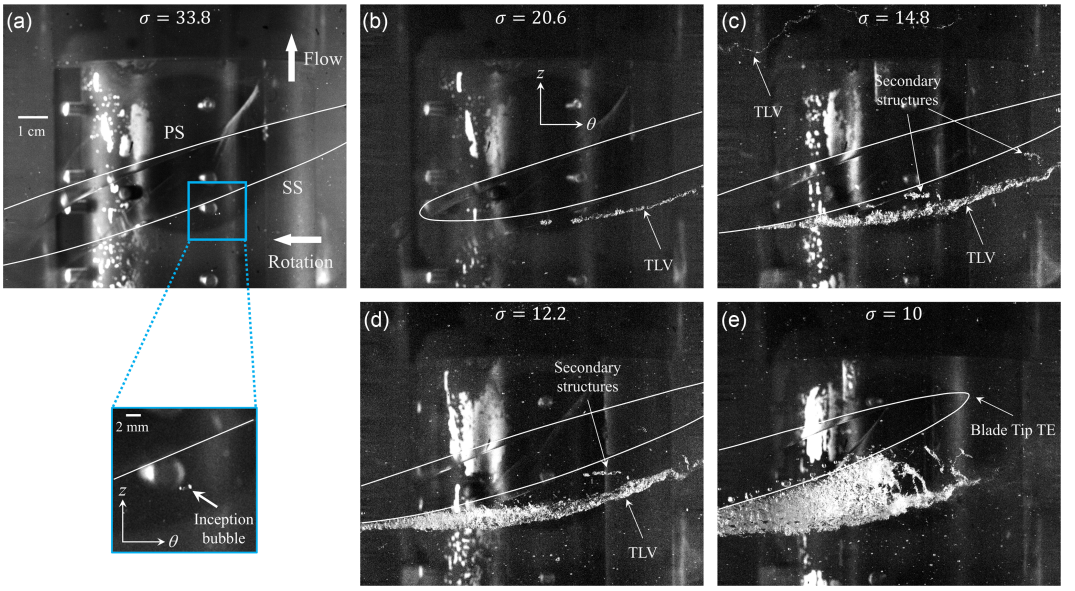

Figure 6. *Sample examples of cavitation for $J = 0.68$: (a) $\sigma = 33.8$, (b) $\sigma = 20.6$, (c) $\sigma = 14.8$, (d) $\sigma = 12.2$, (e) $\sigma = 10$. A magnified view of the region highlighted with a blue box in (a) is shown on the left in the bottom row.*

long, elongated bubbles that are located circumferentially downstream and axially upstream of the blade tip TE. Based on their nearly axial orientation (figure 5(*a*, *d–f*)), these inception events appear to occur in secondary structures and last less than 1 millisecond (figure 5(*d–f*)), consistent with observations reported in Chesnakas and Jessup (2003) for a different propeller. A reduction in σ extends the cavitation to the primary TLV in the region (figure 5(*b*)). Further reduction in pressure extends the cavitation to the entire TLV, and then to travelling bubble cavitation within the blade tip gap, and between the SS of the blade tip and the TLV (figure 5(*c*)). Figure 5(*c*) can also be used for visualising the TLV centre, showing that it rolls up at mid-chord and then migrates away from the blade SS while being aligned in the circumferential direction. The corresponding video, supplementary movie 2, also demonstrates the presence of multiple secondary vortices (presumably) that begin to cavitate intermittently only in the vicinity of the TLV. These vortices are located radially above the TLV and oriented perpendicularly to it before wrapping helically around the TLV centre. Collectively, figure 5 and the movies confirm that cavitation inception indeed occurs in the nearly axial secondary structures. Furthermore, as the secondary structures cavitate only in the vicinity of the TLV, it appears that they are subjected to TLV-induced stretching, which reduces the pressure in their core. A similar evolution of incipient phenomena is observed at $J = 0.933$ (not shown), except for differences in the location of TLV rollup and trajectory, as demonstrated later.

Figure 6 shows the evolution of cavitation at $J = 0.68$, an off-design case, with decreasing σ. The inception bubble (figure 6(*a*), and its enlarged view in the figure inset) forms in the mid-chord region and appears to be oriented along the TLV axis, circumferentially and axially upstream of the blade tip TE. A reduction in pressure expands the cavitation, first to part (figure 6(*b*)), and then to the entire TLV trajectory and secondary vortices entrained by it (figure 6(*c*)). Compared with design conditions, at this J, the TLV rollup begins at a lower s/c, and the secondary structures appear circumferentially upstream as well as downstream of the TE. Travelling bubble cavitation in the tip gap, expansion of the cavitating secondary vortices and filling of the space between the SS tip and the TLV start to occur at $\sigma = 12.2$ (figure 6(*d*)). At this stage, the cavitating TLV is located farther from the blade SS, indicating that cavitation also alters the flow field in the tip region. Further reduction in pressure alters the entire cavitation structure, with the cavitating TLV disappearing and being replaced by multiple large and violent vortices

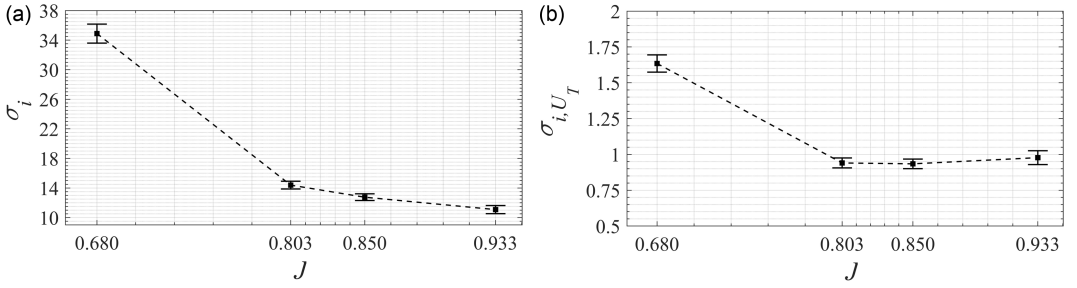

Figure 7. *Cavitation inception index for varying J: (a) σ_i scaled using V_z; (b) σ_{i,U_T} scaled using U_T.*

extending over a broad area (figure 6(*e*)). Figure 7 shows the cavitation inception indices for different *J*, scaled using V_z (σ_i, figure 7(*a*), and U_T (σ_{i,U_T}, figure 7(*b*)). The displayed values correspond to the pressure below which cavitation is first observed at least once every two rotations of the machine. The error bars account for the uncertainties in pressure, velocity, as well as the standard deviation among multiple tests involving both blades. With decreasing J, inception occurs at a higher pressure, resulting in higher σ_i. However, when scaled with the varying U_T, σ_{i,U_T} flattens at about 0.95 for all the data obtained at $J \geq 0.80$, within the uncertainty level. The current values of σ_i are 40%, 17% and 7% lower than those reported by Michael *et al.* (2024) for $J = 0.80$, 0.85 and 0.93, respectively, at an order of magnitude higher *Re*.

3.2. Ensemble-averaged flow structure at design advance ratio

The section describes the mean flow structure at $J = 0.85$, as deduced from the phase-locked and the high-speed SPIV datasets, focusing on the origin and evolution of prominent flow features. Distributions of the ensemble-averaged circumferential vorticity, $\langle\omega_\theta\rangle/\Omega$, where $\omega_\theta = (\partial u_r/\partial z - \partial u_z/\partial r)$, in nine meridional planes (figure 3(*b*)), calculated using the higher resolution phase-locked SPIV data, are presented in figure 8. Note the difference in the axial extents of the FOV between the left and right columns. This figure also contains the in-plane ensemble-averaged velocity vectors (U_r, U_z), with their spacing diluted by 2:1 in r and 3:1 in z for clarity. Plots of the ensemble-averaged circumferential velocity (U_θ/U_T) at $s/c = 0.75$, 1.00 and 1.13, calculated from the same dataset, are presented in figure 9. At the LE ($s/c = 0.00$, figure 8(*a*)), the flow within the tip gap is still from the SS to the PS, whereas at $s/c \geq 0.25$, as tip leakage begins, it is directed from the PS to the SS. Rollup of a TLV begins at around mid-chord ($s/c = 0.50$, figure 8(*c*)), with the appearance of a positive vorticity peak and flow swirling near the SS tip. At $0.75 \leq s/c \leq 1.00$, the TLV grows and migrates away from the SS, while remaining 'connected' to the blade tip by a shear layer that defines the lower boundary of the backward leakage flow. Throughout its trajectory, the TLV centre is located in regions of both elevated magnitude and radial gradients of U_θ (figure 9(*a–c*)), indicating that this vortex is a 3-D swirling jet. Similar phenomena have been seen for TLVs of axial waterjet pumps (Wu *et al.,* 2011a) and aviation compressors (Li *et al.,* 2019; Saraswat *et al.,* 2025). The mechanisms affecting the TLV migration, which include flow induced by the leakage jet during early phases, and by the 'image vortex' on the other side of the endwall in the aft part of the rotor, are characterised in detail by Li *et al.* (2019).

Starting from $s/c = 0.50$ (figure 8*c*), impingement of the backflow on the forward passage flow, above and slightly upstream of the TLV, causes boundary layer separation on the duct wall. This phenomenon results in entrainment of positive vorticity originating from the forward flow boundary layer and negative vorticity from the leakage boundary layer, away from the wall. Driven in part by the TLV-induced flow, the negative vorticity layer is entrained away from the endwall and rolls up into a distinct counter-rotating vortex (CRV), marked with a red arrow in figure 8(*f*). Similar phenomena have been seen in all the ducted axial turbomachines that we have tested, including the above-mentioned waterjet pump and aviation compressors. The locations and strengths of the resulting vortex pairs (TLV and CRV) vary, depending on the blade loading, operating condition, tip gap size, etc.

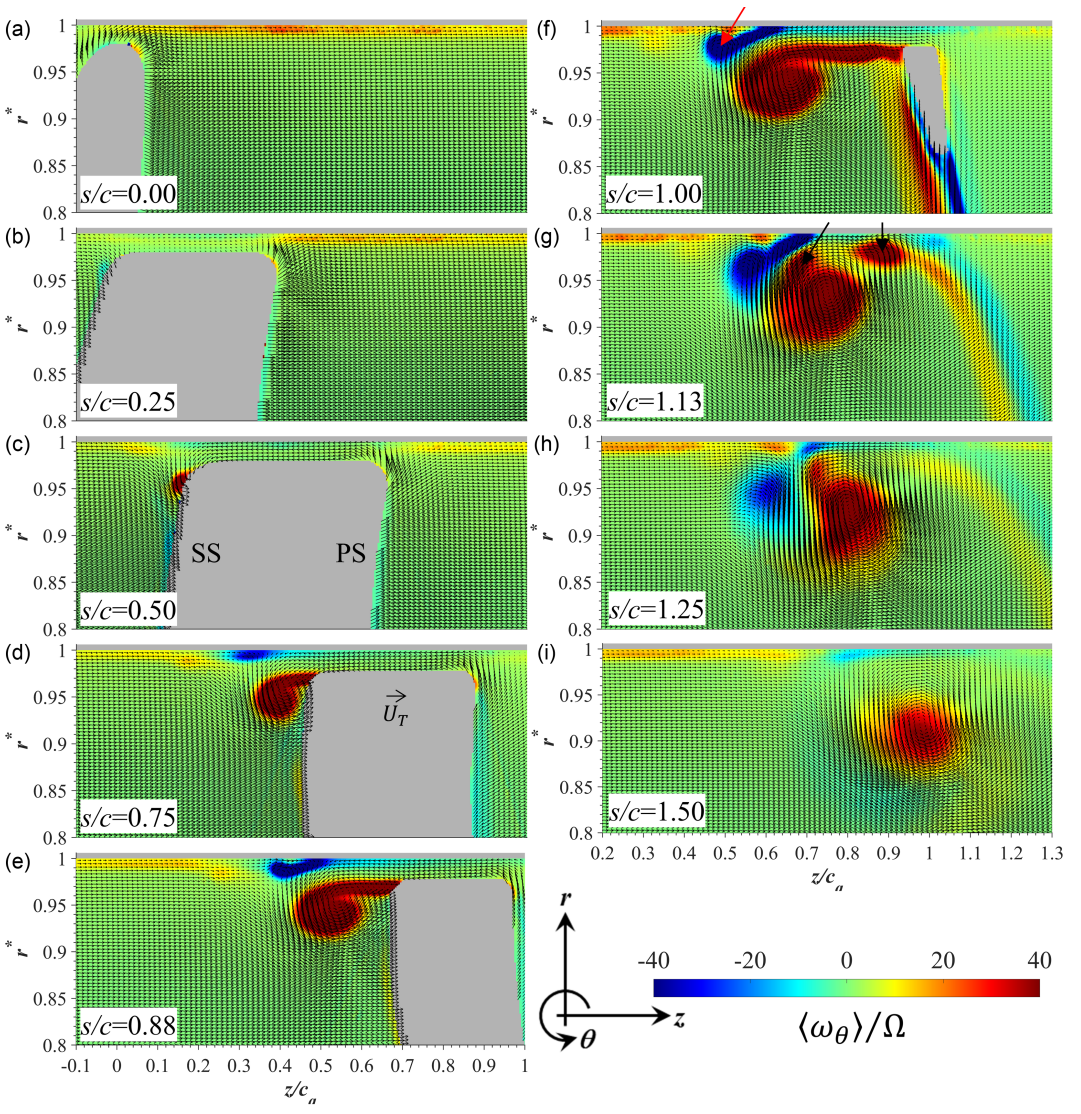

Figure 8. *Distribution of $\langle\omega_\theta\rangle/\Omega$ in nine meridional planes for J = 0.85, calculated using the phase-locked dataset. The superimposed in-plane velocity vectors (U_r, U_z) are shown with their spacing diluted 2:1 in r and 3:1 in z for clarity.*

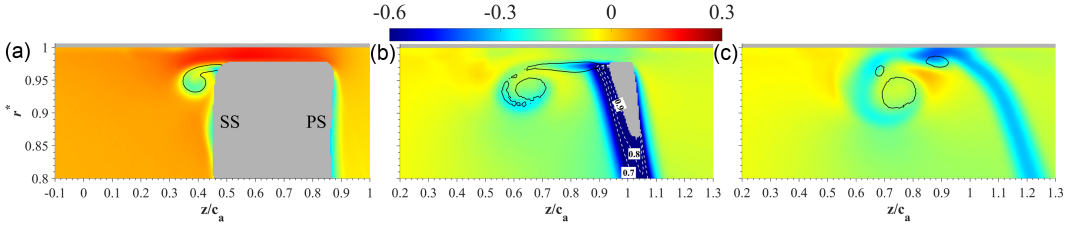

Figure 9. *Distribution of U_θ/U_T for J = 0.85 at (a) s/c = 0.75, (b) s/c = 1.00 and (c) s/c = 1.13. The white dotted lines in (b) highlight the velocity variations within the wake. The black lines in (a–c) are of $\langle\omega_\theta\rangle/\Omega = 40$.*

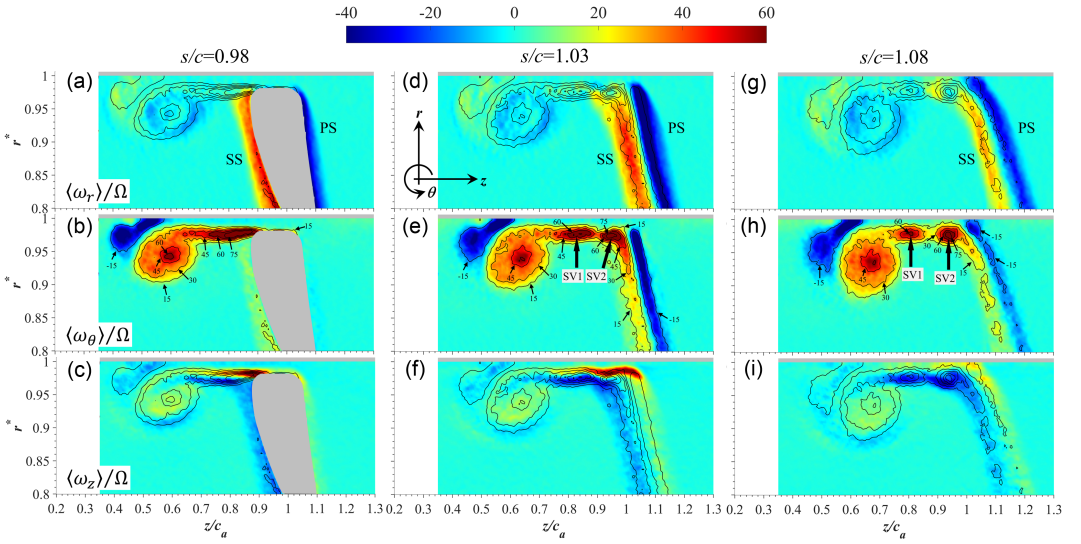

figure 10. *Distribution of ensemble-averaged vorticity components for J = 0.85 calculated from the high-speed dataset at s/c = 0.98 (left), s/c = 1.03 (middle), s/c = 1.08 (right): (a, d, g) $\langle\omega_r\rangle/\Omega$, (b, e, h) $\langle\omega_\theta\rangle/\Omega$, (c, f, i) $\langle\omega_z\rangle/\Omega$. Line contours in all panels are of $\langle\omega_\theta\rangle/\Omega$ marked in the middle row.*

In the forward part of the blade, $\langle\omega_\theta\rangle < 0$ and $\langle\omega_\theta\rangle > 0$ regions form on the blade SS and PS tips, respectively (figure 8(*a*,*b*)). When the TLV is located near the blade SS, shortly after rolling up, the induced radially upward flow below the SS tip corner further augments the negative $\langle\omega_\theta\rangle$ there (figure 8(*d*–*e*)). However, the effect of TLV diminishes as it migrates away from the blade (e.g., figure 8f). In the aft part of the blade ($0.75 \leq s/c \leq 1.00$, figure 8(*d*–*f*)), elevated positive and negative $\langle\omega_\theta\rangle$ layers appear along the blade SS and PS surfaces, respectively, and increase in magnitude close to the TE and in the near wake (figure 8(*f*)). These vortical layers have signs that are opposite to those at the blade tips (figure 8(*d*–*e*)). At $s/c = 1.00$ (figure 8(*f*)), where only the blade tip is visible, the SS contains two opposite-sign vorticity layers. However, circumferentially downstream of the blade (at $s/c = 1.13$, figure 8(*g*)), the negative $\langle\omega_\theta\rangle$ layers originating from the SS and PS merge and become a single continuous layer. The shear layer, located under the backward flow, in figure 8(*g*) also contains two additional secondary vortices (marked with black arrows), that are referred to as SV1 (on the left) and SV2 (on the right) in subsequent discussions. At higher *s/c*, these vortices are entrained into the TLV (e.g., figure 8(*h*)). By $s/c = 1.50$ (figure 8(*i*)), the distinct secondary vortices and the positive vorticity layer associated with the wake and the shear layer are all entrained into the TLV. The remaining broad region with negative vorticity along the upstream periphery of the TLV contains the CRV remnants.

Figure 10 shows sample distributions of all three ensemble-averaged vorticity components, obtained from the lower resolution high-speed SPIV data, in three selected planes, one before ($s/c = 0.98$) and the other two after ($s/c = 1.03$, 1.08) the blade TE. Here, the distributions of $\langle\omega_r\rangle/\Omega$, where $\omega_r = (r^{-1}\partial u_z/\partial\theta - \partial u_\theta/\partial z)$, and $\langle\omega_z\rangle/\Omega$, where $\omega_z = (\partial u_\theta/\partial r - r^{-1}\partial u_r/\partial\theta + u_\theta/r)$, are plotted using the same colour scale as $\langle\omega_\theta\rangle/\Omega$. To facilitate comparisons between components, all the plots also show line contours of specified $\langle\omega_\theta\rangle/\Omega$. For this dataset, the averaging is based on only 114 realisations, hence, the distributions are more 'jittery'. There are also slight differences in the locations of vortices between the two datasets, e.g., an axial shift of $0.03c_a$ in the location of the TLV centre at $s/c = 1.00$, which can be attributed to dissimilar spatial resolutions, interframe times, number of realisations and errors in flow rate. The sample snapshots demonstrate the rapid changes to the flow and vorticity fields near the TE. This evolution is further illustrated in supplementary movies 3-5, which show the mean radial, circumferential, and axial vorticity components, and supplementary movie 6 that displays the mean circumferential velocity. This set enables us to examine the evolution of the 3-D vorticity field.

Starting with the blade surfaces, the pressure gradients between the PS and SS blade tips drive the flow radially up near the PS tip, and then backward across the tip gap. This process generates positive $\langle\omega_\theta\rangle$ on the PS tip corner, and on the blade tip surface (figure 10(*b*)), which becomes the source of the vorticity in the SS tip shear layer and rolls up into the TLV. The blade tip also has layers of $\langle\omega_z\rangle < 0$ along the SS and the underside of the shear layer, and regions of $\langle\omega_z\rangle > 0$ along the PS and the topside of the shear layer (figure 10(*c*)). The latter is associated with radial gradients of U_θ in the boundary layer along the tip gap. Near the TE, this component is comparable in magnitude to $\langle\omega_\theta\rangle$. The negative $\langle\omega_z\rangle$ and the dominant positive $\langle\omega_r\rangle$ layers along the SS surface, and the $\langle\omega_r\rangle < 0$ layer along the PS (figure 10(*a*)) are all associated with the blade boundary layer. The primary contributor to the radial vorticity is $\partial U_\theta/\partial z$ (e.g., figure 9(*b*)). However, due to the slope/tilt of the blade surfaces in the meridional view, part of the boundary layer vorticity is aligned in the axial direction, contributing to $\langle\omega_z\rangle < 0$ in the SS and $\langle\omega_z\rangle > 0$ on the PS. In addition, inherently $\partial U_\theta/\partial r < 0$ along the surface of any blade rotating in the negative θ direction, contributing to $\langle\omega_z\rangle < 0$ on both sides. The combined effects of these two mechanisms result in a slightly positive $\langle\omega_z\rangle$ on the PS, and a negative $\langle\omega_z\rangle$, with a higher magnitude, on the SS. Finally, $\langle\omega_\theta\rangle$ is the smallest near-surface component, but still has positive and negative values on the SS and PS surfaces, respectively (figure 10(*b*)), with the PS values being an order of magnitude lower than those on the SS. The origin of this component is elucidated later.

Just behind the blade, at $s/c = 1.03$ (figure 10(*d–f*)), the 3-D vorticity layers originating from the blade SS and PS surfaces persist in the near wake. The magnitude of $\langle\omega_r\rangle$ remains of the same order as that in the blade boundary layer, but $\langle\omega_\theta\rangle$ increases significantly. As for the vorticity originating from the tip, the positive $\langle\omega_z\rangle$ layer is still evident (figure 10(*f*)). Further behind the blade ($s/c = 1.08$, figures 10*g-i*), all three components of the wake vorticity diffuse, especially the SS wake, and the $\langle\omega_z\rangle > 0$ layer originating from the blade tip gap is advected radially upwards, eventually disappearing at higher s/c. Subsequently (see supplementary movie 5), the distribution of $\langle\omega_z\rangle$ is dominated by the negative layer entrained from the SS side of the blade wake and, to a lesser extent (shown later), tilting of the radial vorticity originated from the SS surface (figure 10(*d*)). The distributions of $\langle\omega_\theta\rangle$ at $s/c = 1.03$ and 1.08 show the presence of SV1 and SV2 (figure 10(*e*, *h*)), that co-rotate with the TLV. To understand their origin, figure 11 (see also supplementary movie 4) shows ensemble-averaged distributions of $\langle\omega_\theta\rangle/\Omega$ in closely spaced planes, focusing on the vicinity of the TE. The origin of SV1 can be traced back to the shear layer separating the backward leakage flow from the forward passage flow radially inward from it (figure 11(*d*)). The source of this vorticity is the blade PS tip corner. In contrast, SV2 starts to roll up circumferentially downstream of the blade, appearing first in the present results at $s/c = 1.02$, and its vorticity appears to largely originate from the blade SS wake (figure 11(*f*)). The distributions of U_θ (supplementary movie 6, or figure 9*b-c*) indicate that both SV1 and SV2 are located in a flow with elevated negative U_θ, which is entrained from the near wake as well as the blade PS upstream of the TE. Hence, describing them as a pair of secondary circumferential vortices underestimates the flow complexity. In reality, similar to the TLV, both SV1 and SV2 are swirling jets.

This paragraph discusses the origin of the $\langle\omega_\theta\rangle$ layers on the blade surface (figure 10(*b*)) that contribute to the formation of SV2. Owing to the no-slip condition, $(1/\rho)\partial p/\partial r \approx {u_\theta}^2/r + \nu\partial\omega_\theta/\partial z$ on the blade surfaces. The second term on the right-hand side represents wall-normal viscous diffusion of vorticity. Since the present geometry is tip loaded by design (Michael *et al.,* 2024), $\partial p/\partial r$ is negative over a substantial fraction of the blade surfaces, especially the SS (except for the vicinity of the TE), resulting in $\partial\omega_\theta/\partial z < 0$ on both sides. Hence, viscous diffusion of vorticity away from the blade surface should add $\langle\omega_\theta\rangle > 0$ to the PS and $\langle\omega_\theta\rangle < 0$ to the SS, both in contrast to the present observations in the aft part of the blade (e.g. figure 10(*b*)). Presumably, either the high-speed SPIV resolution is not sufficient for resolving the inner part of the boundary layers, or other phenomena are stronger. On the PS, the broad low magnitude $\langle\omega_\theta\rangle < 0$ layer starts from the forward part of the blade (figure 8(*b*, *c*)). The primary term contributing to this vorticity, $\partial U_r/\partial z$, is negative outside of the PS boundary layer. In this region, there is radially outward flow, which diminishes away from the blade, as demonstrated by the velocity vectors in figure 8(*c–e*). This outward flow is entrained into the tip gap, suggesting that it is pressure driven. The origin of the negative vorticity is located in the forward part or upstream of

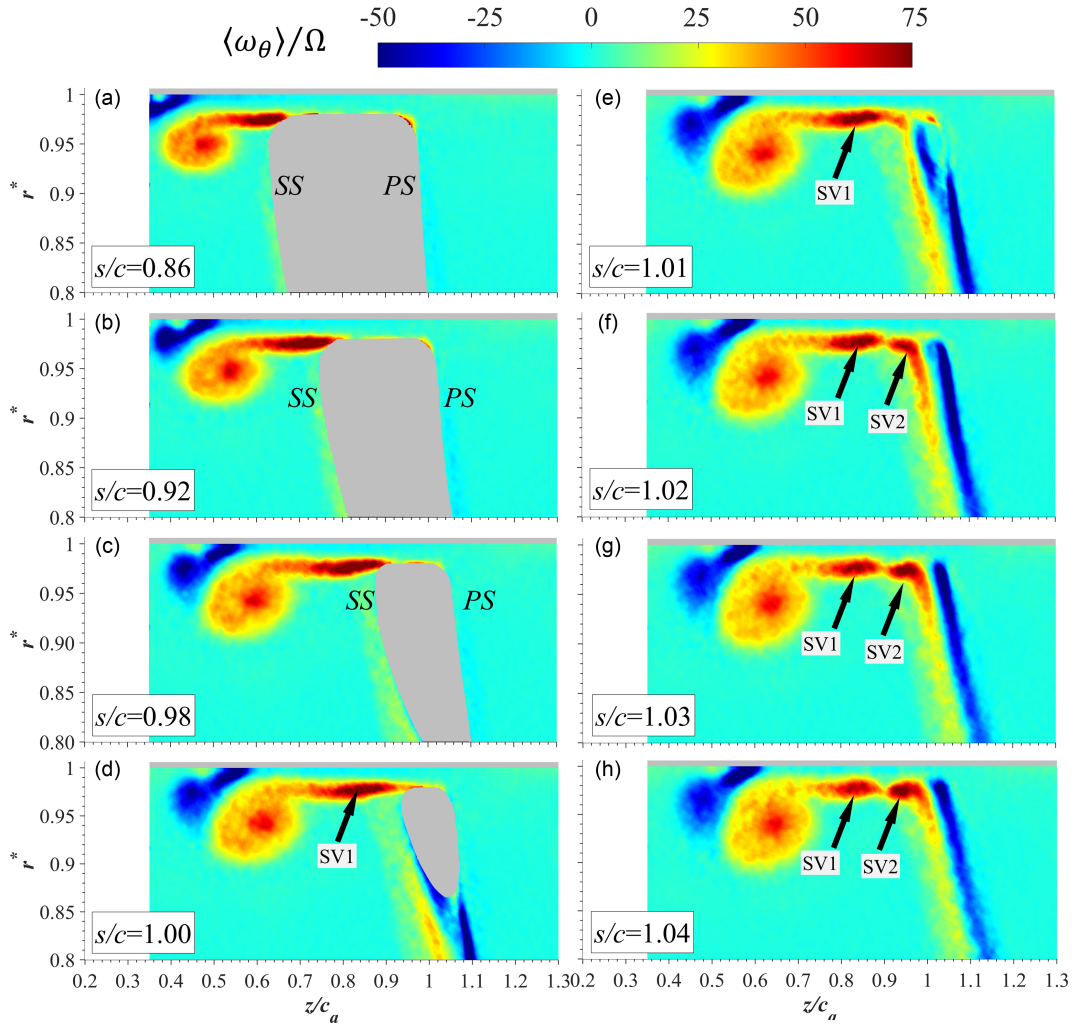

Figure 11. *Distributions of $\langle\omega_\theta\rangle/\Omega$ in closely spaced s/c locations near the blade TE tip for J = 0.85, calculated using the high-speed dataset.*

the blade. Considering that similar layers appear in other axial turbomachines with varying load distributions (Li *et al.,* 2019), the mechanism involved apparently occurs in all of them. One of the potential sources is the axial flow in the hub boundary layer, where $\langle\omega_\theta\rangle < 0$. Shifting to the SS, the origin of the $\langle\omega_\theta\rangle > 0$ layer involves the tilting of other components by the mean flow, such as the reorientation of $\langle\omega_z\rangle$ associated with $\langle\omega_z\rangle\partial U_\theta/\partial z$, or tiling of $\langle\omega_r\rangle$, caused by $\langle\omega_r\rangle\partial U_\theta/\partial r$. Figure 12 shows the distribution of the relevant terms at several *s/c*. In the aft part of the blade SS, e.g., at *s/c* = 0.92, the two tilting terms have opposite signs, but their sum is positive (figure 12(*a*)). In addition, figure 12(*b*) shows that $\langle\omega_\theta\rangle$ is subjected to circumferential stretching ($\langle\omega_\theta\rangle r^{-1}\partial U_\theta/\partial\theta > 0$) by the mean flow on the SS. Being much higher than the tilting terms, such stretching should be a major contributor to the increase in $\langle\omega_\theta\rangle$ near the TE. Finally, there are two possible sources for the $\langle\omega_\theta\rangle < 0$ layer that increase in thickness near the SS TE. The first is viscous diffusion associated with the radial pressure gradients, as discussed above. The second is the radial outward flow induced by the TLV near the tip corner, which occurs only after the vortex rolls up (figure 8(*d–e*)). Consequently, the SS TE contains two vorticity layers with opposite signs. Such multi-layered SS vorticity has been observed experimentally by Chesnakas and Jessup (2003), and computationally by Leasca *et al.* (2024) in another propeller, i.e., it is not unique to the present geometry.

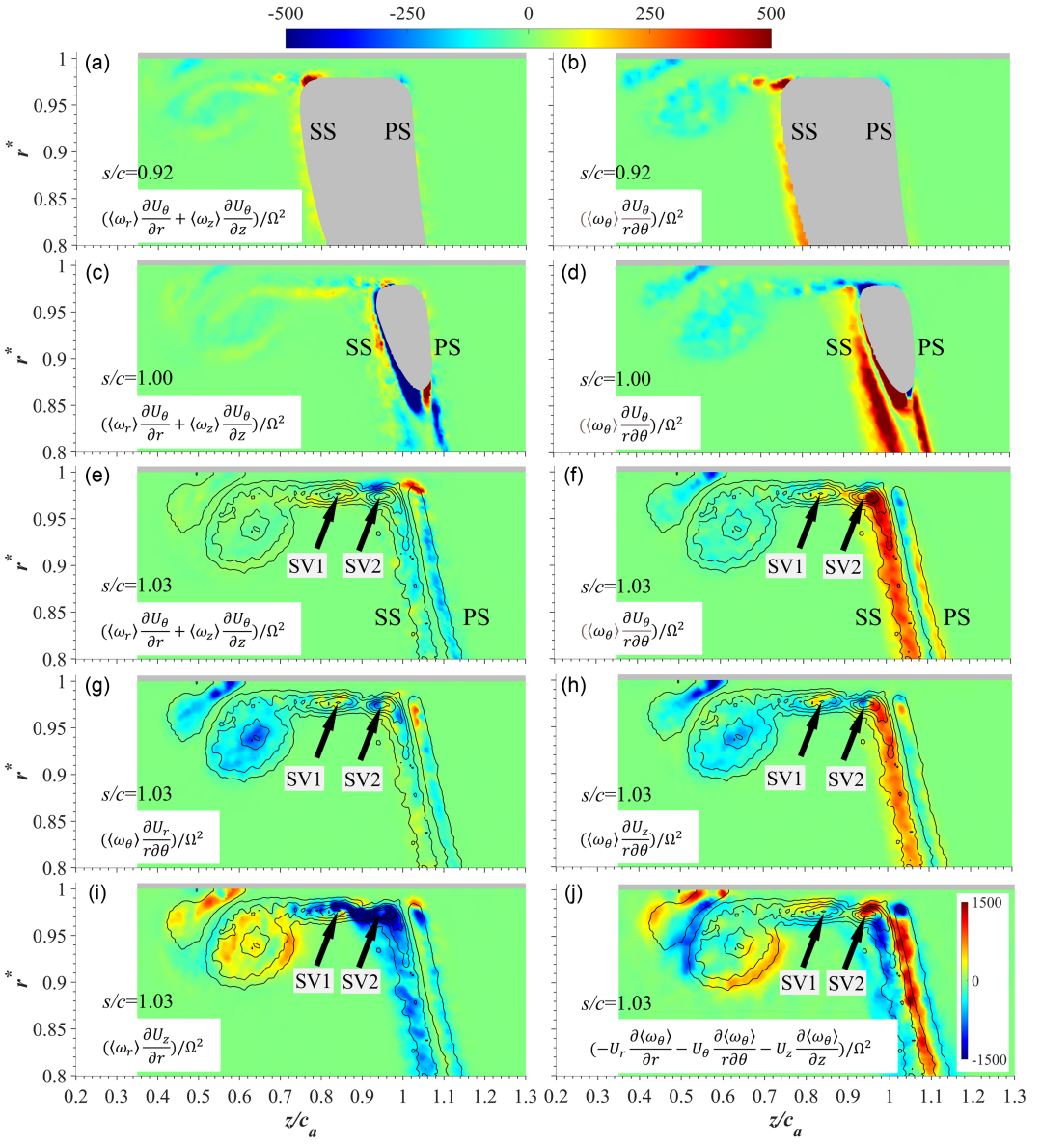

Figure 12. *Distribution of tilting, stretching and advection of vorticity components by the mean flow for J = 0.85 at (a, b) s/c = 0.92, (c, d) s/c = 1.00, (e–j) s/c = 1.03. Definitions of each term are provided on the individual panels. The line contours of* $\langle\omega_\theta\rangle/\Omega$ *at s/c = 1.03 match those in figure 10(d–f). Colour scale for panels (a–i) is provided on top, and as a separate inset for (j).*

As mentioned before, in the near wake, the $\langle\omega_\theta\rangle < 0$ layers from both sides of the blade merge, leaving only two distinct layers with opposite signs (e.g. figure 11(*f*)). Strong circumferential stretching of the $\langle\omega_\theta\rangle > 0$ layer (figure 12(*d*, *f*)) persists up to the region where SV2 first appears, contributing to the increase in $\langle\omega_\theta\rangle$, and overcoming the opposing effects of tilting (figure 12(*e*, *g–h*)). The circumferentially aligned SV1 and SV2 partially overlap with the perpendicular negative $\langle\omega_z\rangle$ layer (figure 10(*h*, *i*)). The latter originates mostly from the blade SS (figure 10(*c*)), but as demonstrated in figure 12(*i*), it is also affected by tilting of the positive $\langle\omega_r\rangle$ layer generated in the blade SS boundary layer. However, the peaks of $\langle\omega_\theta\rangle$ and $\langle\omega_z\rangle$ in these secondary vortices do not coincide, with the latter occurring radially inward from the former. This lattice of vortices is of particular importance since, as demonstrated later,

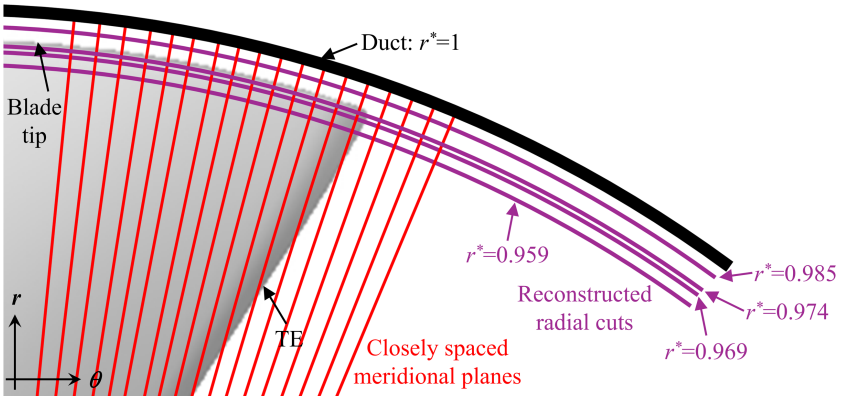

Figure 13. *Illustration of reconstructed radial cuts (constant r^*) from closely spaced meridional planes in the high-speed dataset. Locations of four specific radial cuts are indicated.*

cavitation inception preferentially occurs in the negative $\langle\omega_z\rangle$ layer, especially in the region where the axial vorticity is stretched axially by the flow induced by the TLV as well as by SV1 and SV2. Before proceeding, it should be noted that figures 10 and 12, and supplementary movies 3–5 show numerous other phenomena affecting the evolution of the TLV, such as strain-induced reorientations of $\langle\omega_r\rangle$ and $\langle\omega_z\rangle$ layers, entrainment and merging of vortices, and non-uniform advection by the mean flow (e.g., figure 12(*j*)). Several of these interactions are described in Wu *et al.* (2011*b*) and Li *et al.* (2019) for other axial turbomachines. While they also occur in the present propeller, they are not repeated here to maintain brevity, as we restrict ourselves to phenomena affecting cavitation inception.

3.3. Comparison between mean flow structure and cavitation inception at design advance ratio

Aimed at identifying the physical mechanisms governing the onset of cavitation, this section compares the measured flow field to the observed location of cavitation inception at $J = 0.85$. By combining results obtained in the closely spaced meridional planes of the high-speed dataset, one can reconstruct the flow structure along radial cuts (constant r^*) as illustrated in figure 13. Sample cuts selected for demonstrating trends are $r^* = 0.985$, which is located radially above the blade tip, as well as $r^* = 0.974$, 0.969 and 0.959, which intersect with the blade tip. For reference, the blade tip extends to $r^* = 0.979$. Figure 14 shows the distributions of $\langle\omega_\theta\rangle$ and $\langle\omega_z\rangle$ in the near-TE region of the selected radial cuts. Above the blade tip, figure 14(*a*) shows a broad area with elevated $\langle\omega_\theta\rangle$ axially upstream of the SS, which corresponds to the shear layer connecting the SS tip to the TLV (e.g. figure 10(*b*)). This layer also contains two diagonal bands of particularly high $\langle\omega_\theta\rangle$ that corresponds to SV1 and SV2. Both start near the TE and extend axially upstream and circumferentially downstream of it. The shear layer vorticity peaks at $r^* = 0.974$ (figure 14(*c*)) and decreases further inwards. At $r^* = 0.959$, the signatures of SV1 and SV2 diminish, leaving the TLV as the most prominent structure (figure 14(*g*)). The negative $\langle\omega_\theta\rangle$ layer axially upstream of the TLV, which persists in all the distributions, corresponds to the signature of the separating duct boundary layer and rollup of the CRV. Prominent features in the distribution of $\langle\omega_z\rangle$ include: (i) the positive region associated with the blade tip (figure 14(*b*)) and PS (figure 14(*b*, *d*, *f*, *h*)) boundary layers, which extends to the near wake, (ii) the broad negative region originating from the blade SS that persists in lower radial cuts (figure 14(*f*, *h*)), (iii) the previously discussed negative vorticity radially inward from SV1 and SV2 (figure 14(*d*,*f*)), which is advected radially outwards behind the blade (figure 14(*b*)), and (iv) the positive layer along the TLV, which is associated with the alignment of its trajectory (figure 14(*h*)).

All the plots in figure 14 also show white markers indicating the measured locations of cavitation inception events. We have not observed differences between the dataset obtained near the two blades; hence both are included together. As mentioned earlier, while the radial locations of these events cannot

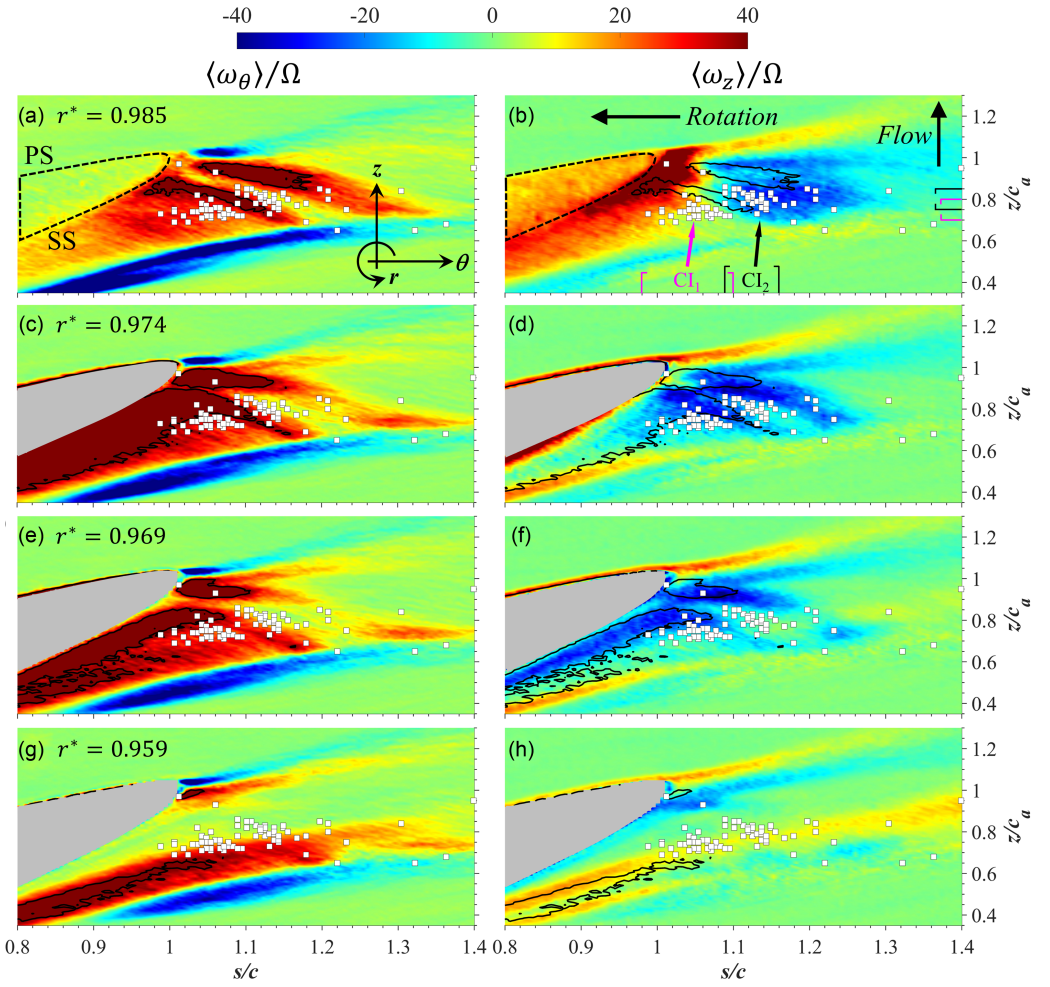

Figure 14. *Distributions of ensemble-averaged vorticity components for $J = 0.85$ in reconstructed radial cuts: (a, c, e, g) $\langle\omega_\theta\rangle/\Omega$, (b, d, f, h) $\langle\omega_z\rangle/\Omega$. Panels show (a, b) $r^* = 0.985$, (c, d) $r^* = 0.974$, (e, f) $r^* = 0.969$, (g, h) $r^* = 0.959$. The black lines are of $\langle\omega_\theta\rangle/\Omega$=40. The white markers denote the s/c and z/c_a locations of inception events. An outline of the blade tip is overlaid on panels (a) and (b).*

be ascertained based on the image recorded by a single camera (figure 2(*a*)), supplementary movie 2 indicates, based on how the cavitating secondary structures wrap around the TLV, that they are located radially outward of the TLV centre. Most of the events appear to be clustered in two different regions. The first group, subsequently referred to as CI_1, is mostly located at $0.98 \leq s/c \leq 1.1$ and $0.70 \leq z/c_a \leq 0.80$, and the second ($CI_2$), at $1.09 \leq s/c \leq 1.16$ and $0.75 \leq z/c_a \leq 0.85$. These ranges agree with those reported for the larger propeller in Michael *et al.* (2024). The left column of figure 14 clearly indicates that these regions do not coincide with the peaks of $\langle\omega_\theta\rangle$ associated with SV1 and SV2. They partially overlap with the region of elevated negative $\langle\omega_z\rangle$ (figure 14, right column), but also do not coincide with the regions of peak vorticity magnitude. In contrast, the right column of figure 15 shows that both CI_1 and CI_2 appear to be concentrated in regions with high magnitude of axial stretching of $\langle\omega_z\rangle$ by the mean flow, i.e. $\langle\omega_z\rangle\partial U_z/\partial z$, but generally do not agree with the location of elevated circumferential stretching of $\langle\omega_\theta\rangle$, i.e., $\langle\omega_\theta\rangle r^{-1}\partial U_\theta/\partial\theta$, shown in the left column. Although, away from the blade, the magnitude of $\langle\omega_\theta\rangle$ is larger than that of $\langle\omega_z\rangle$ (figure 14), $\partial U_z/\partial z$ is significantly larger than $r^{-1}\partial U_\theta/\partial\theta$, especially in the cavitation inception region. More specifically, group CI_2 appears to be co-located better with the

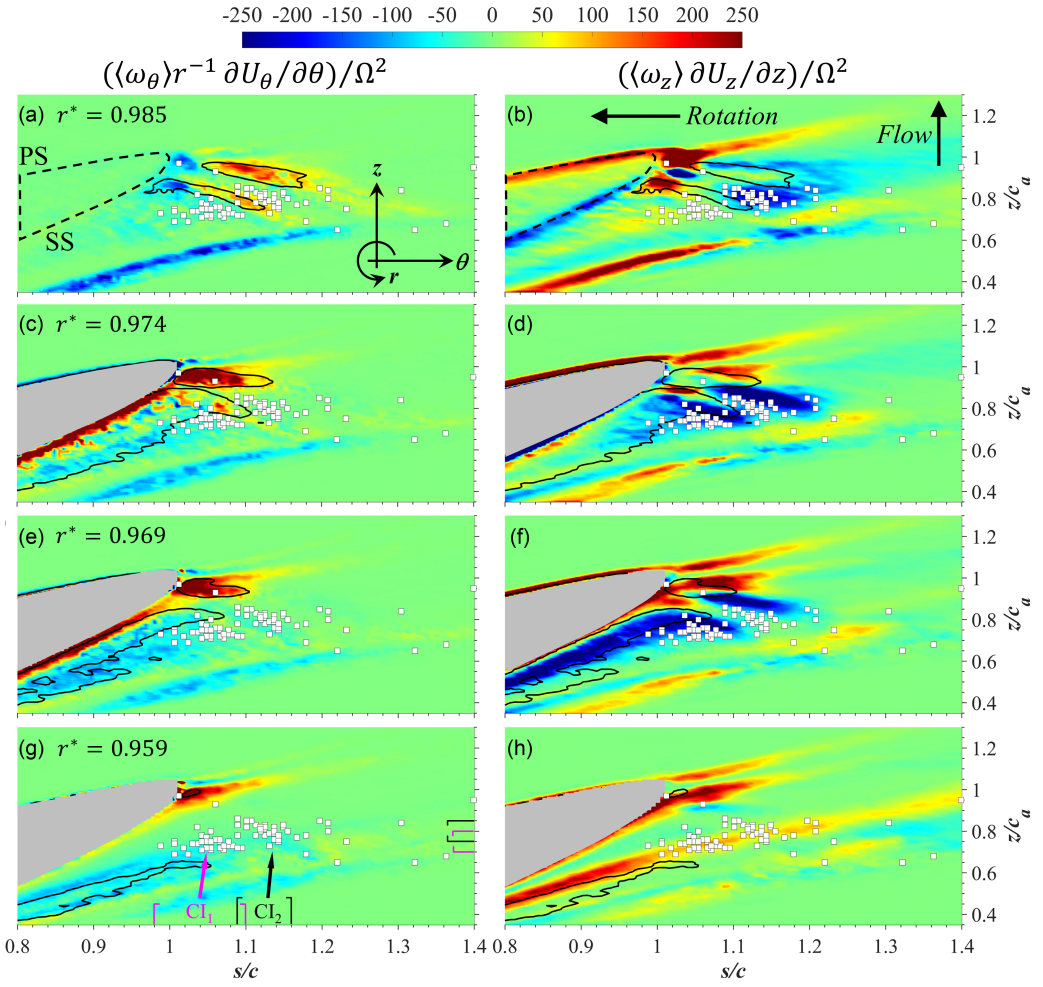

Figure 15. *Distributions of vorticity stretching by mean flow terms for J = 0.85 in reconstructed radial cuts: (a, c, e, g) $(\langle\omega_\theta\rangle r^{-1}\partial U_\theta/\partial\theta)/\Omega^2$, and (b, d, f, h) $(\langle\omega_z\rangle\partial U_z/\partial z)/\Omega^2$. Panels show (a, b) r^* = 0.985, (c, d) r^* = 0.974, (e, f) r^* = 0.969, (g, h) r^* = 0.959. Colour contours are 3 × 3 median-filtered for display. The black lines are of $\langle\omega_\theta\rangle/\Omega$=40. White markers denote the s/c and z/c_a locations of inception events. An outline of the blade tip is overlaid on panels (a) and (b).*

stretching peak at r^* = 0.985 (figure 15(*b*)), i.e., above the blade tip, and CI_1 is better co-located with the stretching peak at r^* = 0.974 and 0.969 (figure 15(*d*, *f*)).

Further clarification of the mechanisms involved is provided in figure 16. This plot highlights $\langle\omega_z\rangle\partial U_z/\partial z$ in only those regions where it and $\langle\omega_z\rangle$ are negative, i.e., where the negative axial vorticity is stretched axially, and compares them with contours of $\langle\omega_\theta\rangle$, showing where the TLV, SV1 and SV2 are located, as well as to the area where the magnitude of negative $\langle\omega_z\rangle$ is high. The vertical lines in figure 16(*a*) indicate the axial boundaries of the CI_1 area at *s/c* = 1.05, and those in figure 16(*b*) bound the CI_2 region at *s/c* = 1.13. The four grey horizontal lines correspond to the r^* of the radial cuts presented in figures 13, 14 and 15. As is evident, the peak vorticity stretching in the CI_1 area is located between SV1 and the TLV, and the axial stretching is caused by the opposite axial velocity induced by two vortices. At *s/c* = 1.13, SV1 is already being entrained into the TLV, and its remnants are located above the TLV centre, while SV2 is still distinct. The CI_2 region is now located between SV1 (or the TLV under it) and SV2. In this case, the stretching is induced by the opposite axial flow induced by SV2 on the right, and TLV + SV1 on the left. In summary, both CI_1 and CI_2 regions are stretched axially by

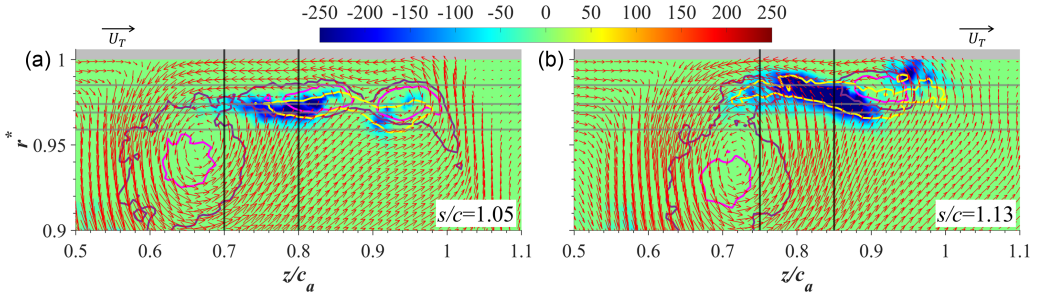

Figure 16. *Distributions of $(\langle\omega_z\rangle\partial U_z/\partial z)/\Omega^2$ in regions where $\langle\omega_z\rangle < 0$ and $\langle\omega_z\rangle\partial U_z/\partial z < 0$ for $J = 0.85$: (a) $s/c = 1.05$, (b) $s/c = 1.13$. Line contours: magenta- $\langle\omega_\theta\rangle/\Omega = 45$, purple- $\langle\omega_\theta\rangle/\Omega = 30$, yellow- $\langle\omega_z\rangle/\Omega = -20$. Grey horizontal lines mark $r^* = 0.985, 0.974, 0.969, 0.959$. The black vertical lines bound the axial extent of CI_1 in (a) and CI_2 in (b). The superimposed in-plane velocity vectors (U_r, U_z) are diluted 2:1 in both r and z for clarity.*

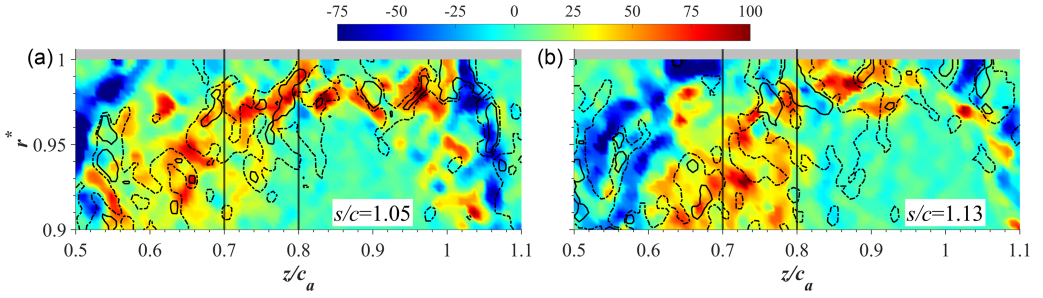

Figure 17. *Samples distributions of 3×3 median-filtered instantaneous circumferential vorticity (ω_θ/Ω) for $J = 0.85$: (a) $s/c = 1.05$, (b) $s/c = 1.13$. The black vertical lines bound the axial extent of CI_1 in (a) and CI_2 in (b). The solid and dashed black lines are of $(\partial u_z/\partial z)/\Omega = 20$ and 5, respectively.*

multiple vortices that are largely aligned in the circumferential direction, but the structures involved are different. As both C1 and C2 regions also have significant magnitude of $\langle\omega_\theta\rangle$, the vortices undergoing stretching are 'quasi-axial' in orientation. Finally, one should keep in mind that figures 14, 15 and 16 still show ensemble-averaged quantities. While one cannot obtain the instantaneous ω_z from the present results, it is still possible to examine the axial straining in the cavitation inception regions. Figure 17 presents sample distributions of 3×3 median-filtered instantaneous ω_θ with superimposed contours of $\partial u_z/\partial z$. The regions where SV1 and SV2 are located contain multiple (circumferential) vorticity peaks, which induce high axial straining in the CI_1 (figure 16(*a*)) and CI_2 (figure 16(*b*)) regions. Similar to the trends of vorticity, the instantaneous axial straining is 3–5 times larger than the ensemble-averaged values. These observations provide motivation for performing volumetric 3-D velocity measurements of straining, 3-D vorticity and pressure, as performed in the regions of cavitation inception, e.g., of a turbulent shear layer by Agarwal *et al.* (2023).

3.4. Effect of advance ratio on the flow structure

This section describes the effect of varying operating conditions on the mean flow features and the resulting changes to the location of cavitation inception in the tip region. Figure 18 compares the distribution of $\langle\omega_\theta\rangle/\Omega$ at $s/c = 0.98$ in the left column, $\langle\omega_\theta\rangle/\Omega$ at $s/c = 1.03$ in the middle column and $\langle\omega_z\rangle/\Omega$ at $s/c = 1.03$ in the right column, for different J values. Figure 19 provides quantitative data on the evolution of several tip flow parameters, all calculated using the high-resolution phase-locked dataset. As is evident from figure 18, the strength and location of the TLV and the CRV vary significantly with J. The mechanisms affecting these trends, which occur to varying extents in all the ducted axial turbomachines

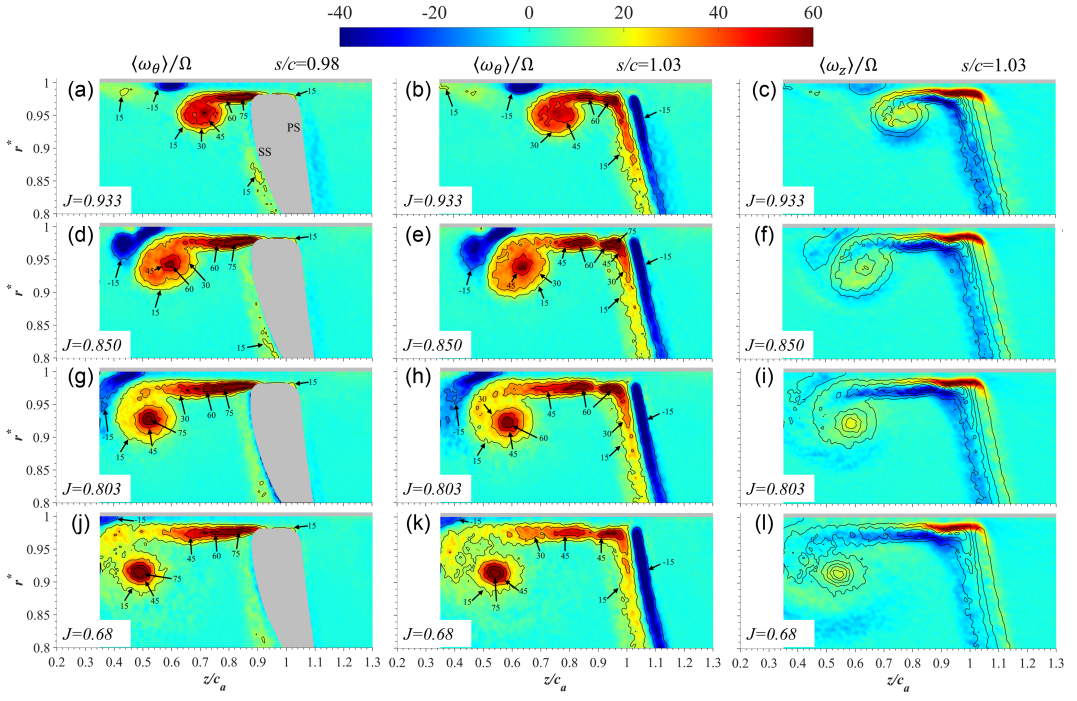

Figure 18. *Distributions of ensemble-averaged vorticity components calculated using the high-speed dataset: (left) – $\langle\omega_\theta\rangle/\Omega$ at s/c = 0.98, (middle) – $\langle\omega_\theta\rangle/\Omega$ at s/c = 1.03, (right) – $\langle\omega_z\rangle/\Omega$ at s/c = 1.03. (a–c) J = 0.933, (d–f) J = 0.85, (g–i) J = 0.803 and (j–l) J = 0.68. Black lines denote the specified values of $\langle\omega_\theta\rangle/\Omega$.*

that we have tested, are associated with differences in blade loading. Consistent with the computational results of Michael *et al.* (2024) and Leasca *et al.* (2024), the latter for a different propeller, with decreasing flow rate, (i) the magnitude of blade loading, hence the strength of the TLV, is expected to increase, and (ii) the point of peak loading, hence the location of TLV rollup, is expected to move closer to the LE. For the present data, at $s/c < 1.00$, calculations of the total positive circulation on the blade SS (Γ_{pos}, figure 19(*a*)) include regions of positive $\langle\omega_\theta\rangle$ around the TLV and the shear layer, at $0.8 \leq r^* \leq 1$. At $s/c \geq 1.00$, SV1, SV2 and the vorticity in the blade SS wake are also included as they are continuously entrained into the TLV. An appropriate threshold, ranging between 2.5% and 5% of the maximum vorticity, is applied to avoid regions associated with the duct boundary layer, as part of it is also entrained into the TLV (figure 8(*d–e*)). To obtain the TLV circulation (Γ_{TLV}, figure 19(*b*)), the shear layer, SV1 and SV2 are not included. Prior to entrainment, these secondary vortices are identified using the local vorticity maxima in their core and the minima between them. Once entrained, these secondary vortices are considered part of the TLV. The expected increase in blade loading with decreasing J agrees with the present distributions of Γ_{pos}, Γ_{TLV} and the peak $\langle\omega_\theta\rangle$ in the TLV (figure 19(*c*)).

Figure 19(*d*) shows that as the TLV evolves, its centre, identified based on the peak of $\langle\omega_\theta\rangle$, migrates away from the blade SS (see also figure 8) at a rate that increases with decreasing J. The point of backflow boundary layer separation also follows similar trends (not shown). To understand the effect of operating conditions, it is shown in Li *et al.* (2019) for an axial compressor that the TLV migration shortly after rollup is dominated by the tip leakage jet, and during later phases, by flow induced by the TLV's 'image vortex' on the other side of the endwall. The present extent of leakage is characterised by radially averaging the velocity across the SS of the tip gap. Figure 19(*f–h*) show the evolution of the axial and circumferential velocity components in the laboratory reference frame ($U_{z,leak}$, $U_{\theta,leak}$), as well as the chord-normal velocity component relative to the blade ($U^*_{n,leak}$), respectively. As is evident, except for the vicinity of the TE, the magnitude of $U_{z,leak}$ and $U^*_{n,leak}$ increase significantly with decreasing J,

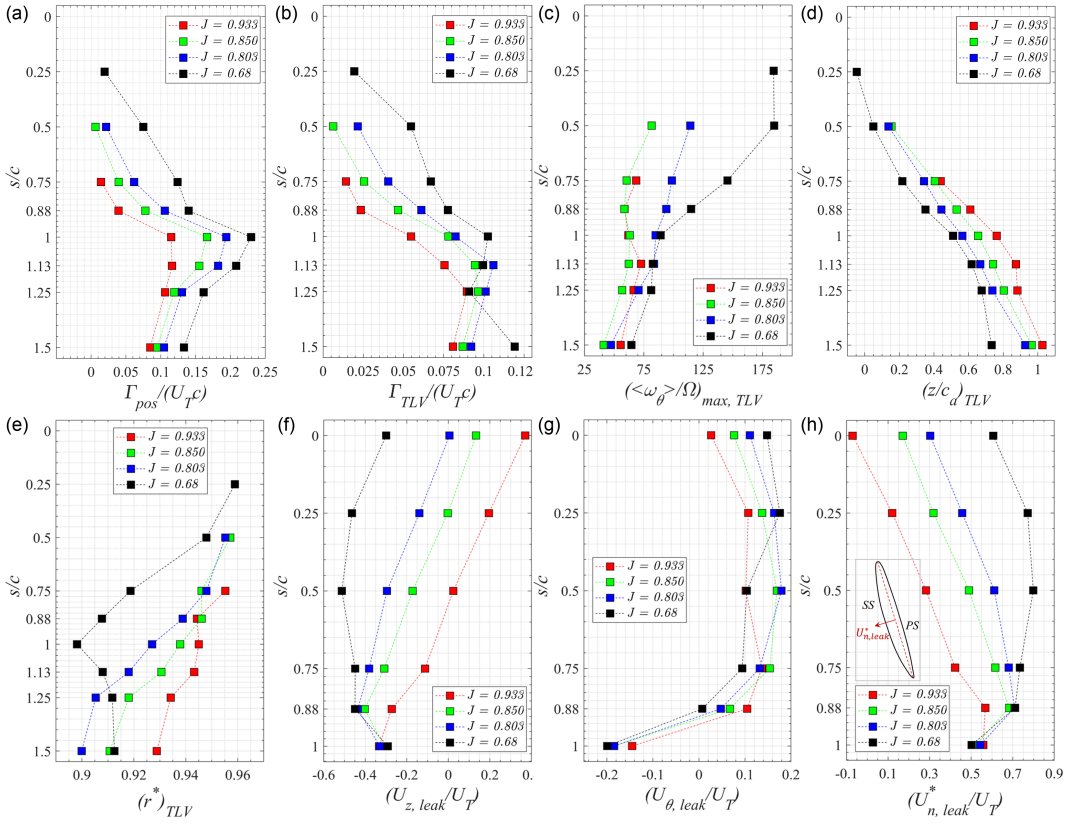

Figure 19. *Effect of advance ratio on the evolution of ensemble-averaged tip flow parameters and TLV location, determined from the phase-locked dataset: (a) total positive circulation shed from the blade SS, $\Gamma_{pos}/U_T c$; (b) circulation within the TLV, $\Gamma_{TLV}/U_T c$; (c) maximum circumferential vorticity in the TLV, $(\langle\omega_\theta\rangle/\Omega)_{max,TLV}$; (d) axial location of the TLV centre, $(z/c_a)_{TLV}$; (e) radial location of the TLV centre, $(r^*)_{TLV}$; (f) radially averaged magnitude of axial velocity at the SS of the tip gap, $U_{z,leak}/U_T$; (g) radially averaged magnitude of circumferential velocity at the SS of the tip gap, $U_{\theta,leak}/U_T$; (h) radially averaged magnitude of chordwise normal velocity component relative to the blade at the SS of the tip gap, $U^*_{n,leak}/U_T$.*

a trend consistent with the increase in blade loading. At $J = 0.68$, $U^*_{n,leak}$ reaches 80% of the U_T at mid-chord, considerably earlier than the ~ 70% peak measured at higher J values. Hence, the earlier and faster leakage jet at the lowest J is expected to push the TLV farther away from the blade. Furthermore, the corresponding higher TLV strength implies that the flow induced by its image is also stronger, affecting the TLV migration in later stages. These observations are consistent with the trends depicted in the left column of figure 18. Figure 19 shows several other interesting phenomena. First, along the blade, the TLV centre migrates further radially inward with decreasing J (figure 19(*e*)). As discussed in Li *et al.* (2019), the likely causes for this trend include flow induced by the negative CRV originating from the separated endwall boundary layer, growth of the TLV, and flow induced by the secondary vortices in the shear layer. The only exception is the trend at $J = 0.68$, where the centre turns radially upwards at $1.0 \leq s/c \leq 1.5$. As supplementary movie 9 and figure 18(*k*) demonstrate, this motion occurs while entrained secondary vortices and the shear layer wrap around the TLV, and are located axially upstream of its centre. Hence, the upward motion might be induced by secondary vortices. Once they are entrained, at $s/c > 1.5$, the radial motion of the TLV centre changes again away from the endwall. Second, for all J values, except near the TE, $U_{\theta,leak}$ is positive, i.e., opposite to the direction of blade rotation (figure 19(*g*)). Furthermore, $U_{\theta,leak}$ increases with s/c until the chordwise location of TLV rollup (figure 19(*a–c*)),

and decreases thereafter. The sign of $U_{\theta,leak}$ is counterintuitive since one would expect that the blade tip motion would induce a flow in the same direction within the narrow tip gap. Such a phenomenon could only be driven by pressure gradients, with the region of PS high pressure located close to the LE, and the SS minimum pressure located at higher s/c, consistent with the results of numerical simulations of this blade (Michael *et al.,* 2024).

Circumferentially downstream of the blade (figure 18, middle column), at least the two co-rotating secondary vortices, referred to earlier as SV1 and SV2, are visible in the shear layer for all the present J values. The mechanisms involved in their formation are similar to those described for $J = 0.85$ and are not repeated here. At $s/c = 1.03$, i.e., close to the TE, vortex SV1 travels slightly further upstream with decreasing J, while the location of SV2 essentially remains unchanged. Their entrainment into the TLV occurs earlier with increasing J (supplementary movies 4 and 7–9), most likely owing to the shorter distance to travel. For the case with the largest distance, $J = 0.68$, both secondary vortices start to break up while still located in the shear layer (supplementary movie 9). Their peak vorticity, which could be used for assessing their strength, appears to have the highest values at design J, and the lowest values occur at $J = 0.68$. The effect of their entrainment into the TLV can also be observed in the evolution of Γ_{TLV} (figure 19(*b*)). While Γ_{pos} decreases at $s/c > 1.00$, Γ_{TLV} continues to increase for the three higher J values, as the TLV entrains the secondary structures. A similar increase in TLV circulation circumferentially downstream of the blade of ducted propellers has been reported in Chesnakas and Jessup (2003) and Oweis *et al.* (2006). At $J = 0.68$, Γ_{TLV} decreases at $1.0 \leq s/c \leq 1.25$, as the TLV begins to break up and spread, but increases again at $s/c > 1.25$, owing to the delayed entrainment of the shear layer and the secondary vortices. The impact of TLV breakup, especially at $J = 0.68$, can also be observed in the rapid reduction of peak $\langle\omega_\theta\rangle$ (figure 19(*c*)) starting from mid-chord, despite the overall increase in TLV circulation caused by the continued entrainment of the shear layer. It should also be noted that the earlier formation, breakup, as well as higher circulation of the TLV with decreasing flow rate have been seen in several other axial turbomachines tested in our facility (Li *et al.,* 2019; Saraswat *et al.,* 2025). With decreasing J, the earlier and stronger TLV also enhances the formation and radially inward entrainment of the CRV originating from the endwall boundary layer (figure 18, left and middle columns). Before concluding this discussion, the right column of figure 18 demonstrates the effect of J on the distributions of $\langle\omega_z\rangle/\Omega$ circumferentially downstream of the blade. All the distributions contain the signature of the positive layer originating from the blade tip and the PS wake, and the negative layer originating from the blade SS which contains the quasi-axial vortices. The peak magnitudes of negative $\langle\omega_z\rangle$ are present in the vicinity of SV1 and SV2, but do not coincide with their $\langle\omega_\theta\rangle$ peaks. Hence, the previously discussed axial stretching of negative $\langle\omega_z\rangle$ is expected to occur in all cases.

Figure 20 shows a comparison between locations of cavitation inception and the ensemble-averaged flow structure for $J = 0.933$. In contrast to design J, most of the events are clustered in a single region located at $1.05 \leq s/c \leq 1.14$ and $0.80 \leq z/c_a \leq 0.90$ (figure 20(*a–c*)). This circumferential extent is in between the CI_1 and CI_2 regions of design J but is axially closer to the blade TE. Here again, the locations of inception appear to have a better agreement with regions of negative $\langle\omega_z\rangle$ and high negative $\langle\omega_z\rangle\partial U_z/\partial z$ (figure 20(*a–c*)). The perpendicular view (figure 20(*d–f*)) highlights the evolution of the stretched negative $\langle\omega_z\rangle$ in the relevant areas. At $s/c = 1.06$, as SV1 is getting entrained into the TLV, the regions containing peaks of both negative $\langle\omega_z\rangle$, highlighted through a yellow line contour, and its stretching are located around both SV1 and SV2, and coincides with the cavitation inception domain highlighted through black vertical lines. At $s/c = 1.09$, the cavitation inception region partially overlaps with the region of peak axial stretching and elevated $\langle\omega_z\rangle$, and the structures involved are the same as those for CI_2 at the design J. At $s/c = 1.12$, SV2 is located radially above the TLV, and the stretched axial vorticity, located to the right of both, still partially overlaps with the inception range. Note that the radial location of peak stretching also changes, implying that events appearing in the same cluster do not necessarily occur at the same r^*.

The locations of cavitation inception for $J = 0.803$ and 0.68 are compared with those observed for higher J values in figure 21. At $J = 0.803$, while some events still appear as axially aligned bubbles at $s/c > 1$, they mostly occur within the TLV, and have a dominant scatter in the range $0.60 \leq s/c \leq 0.90$

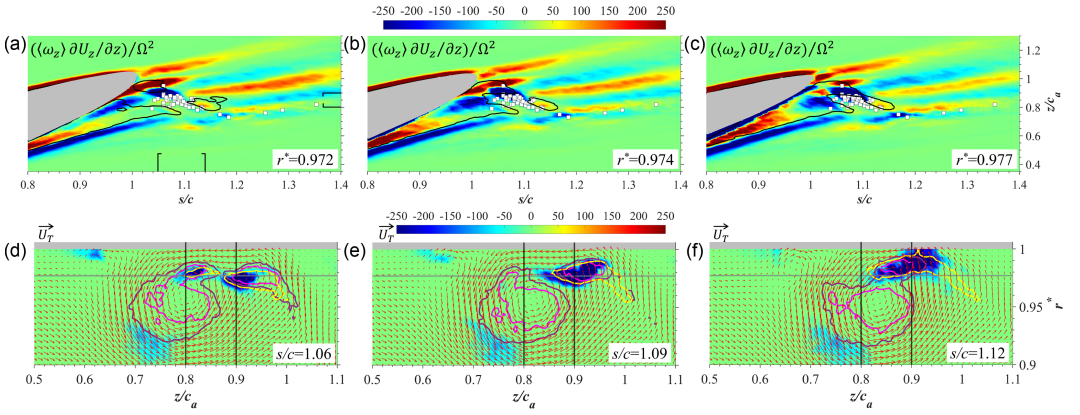

Figure 20. *First row: colour contours of 3 × 3 median-filtered $(\langle\omega_z\rangle\partial U_z/\partial z)/\Omega^2$ for $J = 0.933$: (a) $r^* = 0.972$, (b) $r^* = 0.974$, (c) $r^* = 0.977$. In panels (a–c), black lines are of $\langle\omega_\theta\rangle/\Omega = 40$, and white markers indicate cavitation inception events. Second row: colour contours of $(\langle\omega_z\rangle\partial U_z/\partial z)/\Omega^2$ in regions where $\langle\omega_z\rangle < 0$ and $\langle\omega_z\rangle\partial U_z/\partial z < 0$: (d) s/c = 1.06, (e) s/c = 1.09, (f) s/c = 1.12. In panels (d–f), line contours: magenta- $\langle\omega_\theta\rangle/\Omega = 45$, purple- $\langle\omega_\theta\rangle/\Omega = 30$, yellow- $\langle\omega_z\rangle/\Omega = -20$. Grey horizontal line: $r^* = 0.977$. The black vertical lines bound the axial extent of cavitation inception events shown in panels (a–c). The superimposed in-plane velocity vectors are diluted 2:1 in both r and z for clarity.*

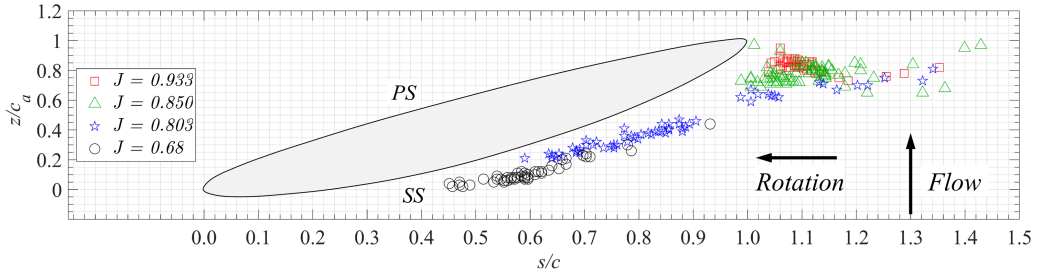

Figure 21. *Distribution of the location of cavitation inception events for various advance ratios.*

along its path. At $J = 0.68$, all the inception events occur along the TLV centre, most of them at $0.45 \leq s/c \leq 0.7$, with the highest concentration centred around $s/c \sim 0.6$. The earlier rollup and higher TLV strength (higher blade loading) with decreasing J appear to shift the location of cavitation inception further circumferentially upstream. The most likely location of inception along the TLV is close to the point of peak $\langle\omega_\theta\rangle$ (figure 19(*c*)), and does not occur at higher *s/c*, despite the increase in TLV circulation (figure 19(*b*)). This trend is presumably associated with the breakup of the TLV core and its fragmentation into multiple vortices along the aft part of the blade. Upon reduction of the mean pressure below the inception level, cavitation also expands to the secondary structures near the TE, in agreement with the persistence of the secondary vortices under all operating conditions (figure 18).

3.5. Discussion

The mean pressure around the blade tip TE is affected by the flow around the blade and the presence of the TLV. The RANS-predicted mean surface pressure distribution reported in Michael *et al.* (2024) shows that the SS blade pressure starts increasing from mid-chord to the aft of the blade. Furthermore, as the pressure increases with increasing distance from the TLV centre, the secondary vortices developing in the vicinity of the blade TE, but away from the TLV, are in a region of elevated mean pressure. This observation implies that the formation of localised regions with very low pressure outside of the TLV core can only occur owing to vortex stretching, and the resulting reduced radius and increased vorticity.

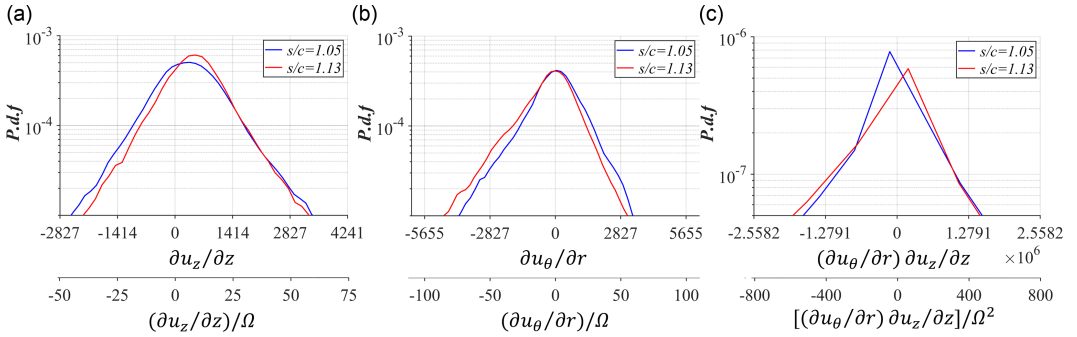

Figure 22. *Probability density functions: (a) axial strain rate $\partial u_z/\partial z$; (b) surrogate axial vorticity $\partial u_\theta/\partial r$; and (c) surrogate axial vortex stretching, $\partial u_z/\partial z(\partial u_\theta/\partial r)$, computed in the region of cavitation inception for J = 0.85. The sampling areas are $r^* > 0.95$ with $0.7 \le z/c_a \le 0.8$ at s/c = 1.05, and $r^* > 0.95$ with $0.75 \le z/c_a \le 0.85$ at s/c = 1.13. The upper horizontal axis shows dimensional values, and the lower horizontal axis shows the same data normalised using Ω (for panels a and b) or Ω^2 (for panel c).*

We have already demonstrated that cavitation first occurs in regions where quasi-axial secondary vortices are stretched axially by the flow induced by the circumferentially aligned TLV and secondary vortices located in the shear layer separating the leakage flow from the main passage flow. This vortex stretching-induced cavitation inception, where a small, weak vortex is elongated by several larger and perpendicular vortices, is not unique to the present propeller flow. Therefore, it is instructive to compare the axial strain rates and vortex stretching magnitudes measured here with those reported in other flows exhibiting the same mechanism, such as turbulent shear flows (Katz & O'Hern 1986; Agarwal *et al.,* 2023). For a turbulent shear layer behind a backward-facing step, Agarwal *et al.* (2023) show that at a flow speed of the same order of magnitude as the current U_T, cavitation first occurs in quasi-streamwise vortices that are stretched by the much larger and stronger spanwise vortices. Their most probable magnitude of axial strain rate is 500–1000 s^{-1} but extends to more than 2500 s^{-1} in extreme cases. The most probable vortex stretching term magnitude, along its axis, is of the order of 10^5. For this propeller, statistics of axial vortex stretching for design J, in the cavitation inception region, i.e., $r^* > 0.95$, and at $s/c = 1.05$, $z/c_a = 0.7$ to 0.8; and $s/c = 1.13$, $z/c_a = 0.75$ to 0.85, are provided in figure 22. Probability density functions (PDFs) of the instantaneous axial straining, $\partial u_z/\partial z$, are presented in figure 22(*a*). The most probable value of ~500 s^{-1} and the peak value of ~3000 s^{-1} are similar in magnitude to those reported in Agarwal *et al.* (2023). Unfortunately, we have not measured the instantaneous ω_z, but the ensemble-averaged data obtained from the time-resolved measurements indicate that the magnitude of $\langle\omega_z\rangle$ is dominated by $\partial U_\theta/\partial r$, i.e. $\partial U_\theta/\partial r \gg (\partial U_r/r\partial\theta + U_\theta/r)$. Hence, we use $\partial u_\theta/\partial r$ as a surrogate for the instantaneous axial vorticity and presents its PDF in figure 22(*b*). As is evident, the magnitude of the negative values is larger, extending to $-4000\ s^{-1}$. Furthermore, the negative surrogate vorticity at $s/c = 1.13$ has a higher magnitude than that at $s/c = 1.05$, as one would expect because of axial vortex stretching. The PDF of the surrogate axial vortex stretching term $(\partial u_\theta/\partial r)\partial u_z/\partial z$, shown in figure 22(*c*), reaches peak negative values of 10^6 which is an order of magnitude higher than the shear layer results of Agarwal *et al.* (2023). This difference explains the higher σ_{i,U_T} (~0.95) for the present propeller than those measured in the shear layer (~0.5).

The following discussion attempts to understand the shift in the location of cavitation inception below design conditions. As shown in the previous sub-section, changing the operating conditions alters the strength of the TLV, as well as the location of its rollup and breakup. Fragmentation of tip leakage vortices and the associated increase in turbulence have been seen in essentially all the ducted axial turbomachines tested in our facility (Wu *et al.,* 2012; Li *et al.,* 2017, Saraswat *et al.,* 2025). The mechanisms affecting the breakdown of vortices under the influence of adverse pressure gradients have been investigated in a variety of flows (e.g., Hall, 1972; Escudier, 1988; Lucca-Negro and O'Doherty, 2001). Inherent to all axial pumps and compressors, there are adverse pressure gradients in the aft part of the

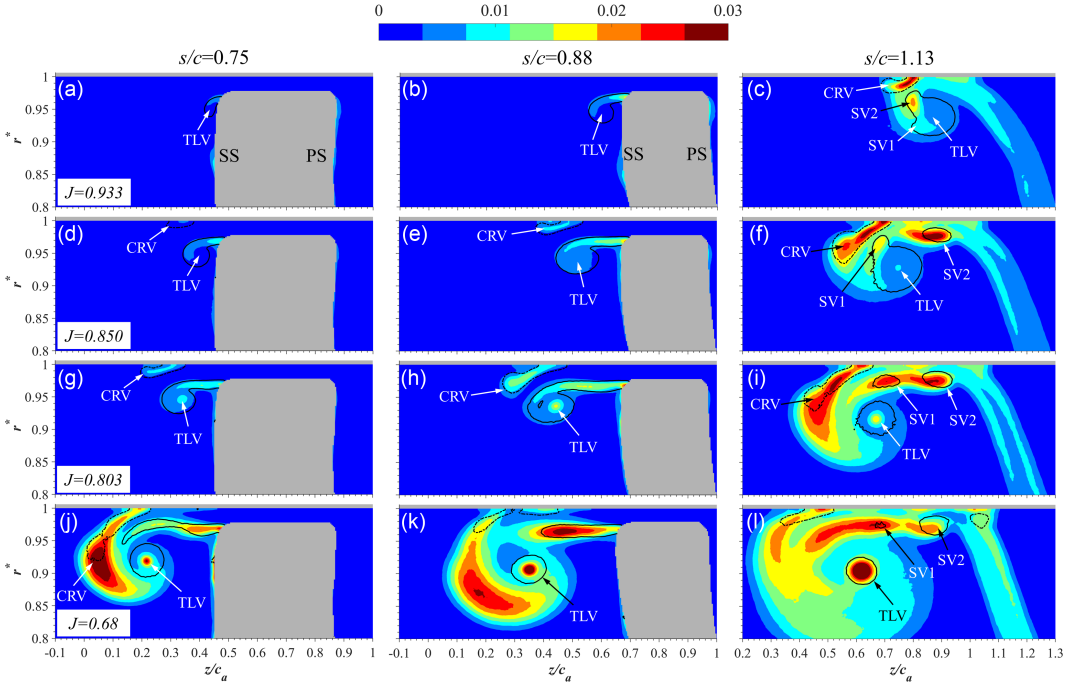

Figure 23. *Effect of advance ratio on the distribution of TKE, k/U_T^2, calculated from the phase-locked dataset at: (left) s/c = 0.75, (middle) s/c = 0.88, (right) s/c = 1.13. (a–c) J = 0.933, (d–f) J = 0.85, (g–i) J = 0.803 and (j–l) J = 0.68. Line contours, solid black: $\langle\omega_\theta\rangle/\Omega = 30$, dashed black: $\langle\omega_\theta\rangle/\Omega = -20$.*

rotor passage. As the TLV migrates to this region, it contracts along its axis, making it unstable and prone to breakdown. Once the so-called "spiral-type vortex breakdown" occurs (Lucca-Negro and O'Doherty, 2001), the TLV starts meandering, and its core fragments into multiple filaments that occupy a growing area. Consequently, the mean vortex size increases and its peak vorticity magnitude decreases. This effect becomes more pronounced below design conditions, where the blade's peak loading and the point of TLV rollup shift towards the leading edge, and the adverse pressure gradients start earlier and become stronger. Consequently, the TLV breakdown occurs earlier, appears to increase in intensity and manifests as an increase in the vortex core's turbulence level. Other mechanisms that affect the breakdown include migration of the TLV to the PS of the neighbouring blade, a phenomenon that is more prominent in multi-blade compressors and pumps, and flow non-uniformities caused by, e.g., other co-, counter-rotating, and even inclined secondary vortices (Lim, 1998; Le *et al.,* 2011). A detailed discussion on the evolution of turbulence is beyond the scope of this paper. However, to demonstrate the effect of TLV breakup, figure 23 compares the distributions of TKE, calculated using the high-resolution, phase-locked dataset, at $s/c = 0.75$, 0.88 and $s/c = 1.13$. Circumferentially upstream of the TE ($s/c = 0.75$ and 0.88), there is strikingly high turbulence at $J = 0.68$ in comparison with the other advance ratios, which is associated with earlier breakdown of vortices. With decreasing J, the regions of elevated turbulence expand from only the shear layer at $J = 0.933$ to the CRV and the vicinity of the TLV at $J = 0.85$, then to the centre of the TLV at $J = 0.803$, and finally to a broad area with much higher values at $J = 0.68$. For $J = 0.68$, the TKE is particularly high in the shear layer, the TLV centre and the entrained separated backflow boundary layer. At $s/c = 1.13$, the areas with elevated turbulence expand in all cases, with additional peaks appearing in the vicinity of SV1, SV2 and the blade wake. The regions of cavitation inception at $J = 0.933$ and 0.85, which are between the TLV and SV1, and between SV1 and SV2, are not characterised by particularly high turbulence. This observation indicates that the onset of cavitation preferentially occurs in regions where the flow structure is at least 'quasi-coherent'. For the cases

where the vicinity of SV1 and SV2 becomes turbulent, i.e., the lower two J values, the cavitation inception events shift to the TLV. These observations are also consistent with measurements of cavitation inception in turbulent shear layers (Agarwal *et al.,* 2023), where the likely inception site is in a domain where secondary vortices are quasi-coherent, upstream of the regions with maximum turbulence level. A similar trend is observed along the TLV core, where inception occurs closer to the TE at $J = 0.803$, but at $J = 0.68$ shifts further upstream along the TLV, circumferentially before the TLV breakdown, as indicated by a reduction in peak $\langle\omega_\theta\rangle$ (figure 19(*c*)) and elevated turbulence near its centre.

4. Conclusions

The present study characterises the onset of cavitation and the associated flow structure in a ducted propeller at varying advance ratios. At design and higher advance ratios, cavitation inception appears as axially aligned intermittent cavities that form axially between the blade SS and the TLV, and circumferentially at $0.98 < s/c < 1.16$, i.e., downstream of the blade TE. Further reduction in mean pressure reveals that the inception occurs in secondary vortices aligned perpendicularly and radially above the TLV. With decreasing advance ratio, the cavitation inception indices defined using the mean axial velocity increase, and their most probable location shifts first to the TLV, and then along its core towards the blade leading edge. Scaling the cavitation inception indices with the blade tip speed gives a value of ~0.95 for all near-design conditions. Two SPIV datasets are used for characterising the evolution of the non-cavitating flow structure around the blade tip. Higher-resolution data covering the entire blade axial chord are obtained in discrete meridional planes, starting from the leading edge and extending beyond the TE, encompassing the entire cavitation inception area. This dataset captures the formation and evolution of the tip leakage flow, the blade near wake, the TLV and several counter- and co-rotating secondary vortices that remain distinct in the ensemble-averaged data. The second SPIV dataset is recorded at 30 kHz, but at a lower spatial resolution and smaller sample area. Owing to the closely spaced meridional planes, this dataset enables calculation of all three mean vorticity components in the vicinity of the TE, hence captures the axial vortices causing cavitation inception.

The prominent flow features in the tip region include the leakage flow, the rollup, evolution and breakup of the TLV, and the formation of circumferentially aligned secondary vortices in the near wake. These secondary vortices, referred to as SV1 and SV2 in the mean flow, co-rotate with the TLV and are eventually entrained into it. Vortex SV1 rolls up in the shear layer that connects the TLV to the SS tip and separates the passage flow from the backward leakage flow. The source of its vorticity, like the TLV, is the blade PS tip corner. In contrast, vortex SV2 starts to roll up circumferentially downstream of the blade. The vorticity in SV2 largely originates from the blade SS wake due to realignment of the axial vorticity generated on the blade surface and is subsequently stretched circumferentially near the TE. In addition, positive and negative quasi-axial vortices originating from the blade pressure and suction sides, respectively, are continuously shed and entrained into the vicinity of the shear layer. At high advance ratio, including the design conditions, cavitation inception occurs in the region where the negative quasi-axial vortices are stretched axially by the flow field induced by the circumferential TLV, SV1 and SV2. The straining mechanisms are qualitatively similar to the axial stretching of quasi-streamwise vortices in a 2-D shear layer by the opposite induced flow of the primary spanwise vortices. The extent of vortex stretching observed in the tip region is an order of magnitude higher than that measured in the 2-D shear layer studies. Several mechanisms contribute to the shift of the cavitation inception site to the TLV and towards the leading edge with decreasing advance ratio. First, with increasing blade loading, the TLV rolls up earlier and increases in strength. Hence, its core pressure is likely to decrease, resulting in higher cavitation inception indices. Second, the TLV breaks up earlier in the aft part of the blade, resulting in its fragmentation and loss of its distinct dominant core. The signature of this breakup in the mean flow structure appears as a sharp decrease in peak vorticity, despite a continued increase in overall circulation, and an increase in turbulence level along the vortex core. Finally, a comparison of the TKE distributions demonstrates that, at all conditions, cavitation inception preferentially occurs in regions located away

from the peaks in turbulence level, i.e., where the flow structure is at least 'quasi-coherent', even in the case of off-design condition. Owing to the flow complexities, the present findings motivate shifting the focus to volumetric time-resolved measurements, which will enable us to characterise the evolution of instantaneous vorticity and the dynamic pressure field in the regions of cavitation inception.

Supplementary material. The supplementary material for this article can be found at https://doi.org/10.1017/flo.2025.10026.

Acknowledgments. The authors would like to thank Dr. Thad Michael from the Naval Surface Warfare Center Carderock Division (NSWCCD) for designing and sharing the propeller blade geometry. We would also like to express our gratitude to the late Dr. Yury Ronzhes who led the designing and fabrication of the turbomachine facility and the current experimental set-up.

Data availability statement. Data will be made available upon reasonable requests.

Author contributions. A.S. and C.P. assembled the test facility. A.S., C.P. and K.S. performed the experiments. A.S. performed the analysis. A.S. and J.K. wrote the manuscript. J.K. supervised the study.

Funding statement. This work has been supported by the Office of Naval Research (ONR) under grant number N00014-21-1-2833. The program officer is Dr. Yin Lu (Julie) Young.

Declaration of interests. The authors declare no conflict of interest.

Ethical standards. The research meets all ethical guidelines, including adherence to the legal requirements of the study country.

References

Agarwal, K., Ram, O., Lu, Y., & Katz, J. (2023). On the pressure field, nuclei dynamics and their relation to cavitation inception in a turbulent shear layer. *Journal of Fluid Mechanics*, *966*, A31.

Arndt, R. E. A. (2002). Cavitation in vortical flows. *Annual Review of Fluid Mechanics*, *34*(1), 143–175.

Arndt, R. E. A., Arakeri, V. H., & Higuchi, H. (1991). Some observations of tip-vortex cavitation. *Journal of Fluid Mechanics*, *229*, 269–289.

Bai, K., & Katz, J. (2014). On the refractive index of sodium iodide solutions for index matching in PIV. *Experiments in Fluids*, *55*, 1704.

Benedict, L. H., & Gould, R. D. (1996). Towards better uncertainty estimates for turbulence statistics. *Experiments in Fluids*, *22*(2), 129–136.

Boulon, O., Callenaere, M., Franc, J.-P., & Michel, J.-M. (1999). An experimental insight into the effect of confinement on tip vortex cavitation of an elliptical hydrofoil. *Journal of Fluid Mechanics*, *390*, 1–23.

Brandao, F. L., Kumar, P., & Mahesh, K. (2024). Large-eddy simulation of elliptic hydrofoil tip vortex cavitation under incipient conditions. *Int. J. Multiphase Flow*, *174*, 104795.

Chang, N. A., Choi, J., Yakushiji, R., & Ceccio, S. L. (2012). Cavitation inception during the interaction of a pair of counter-rotating vortices. *Physics of Fluids*, *24*(1), 014107.

Chang, N. A., Yakushiji, R., Dowling, D. R., & Ceccio, S. L. (2007). Cavitation visualization of vorticity bridging during the merger of co-rotating line vortices. *Physics of Fluids*, *19*(5), 058106.

Chen, H., Li, Y., Tan, D., & Katz, J. (2017). Visualizations of flow structures in the rotor passage of an axial compressor at the onset of stall. *Journal of Turbomachinery-Transactions of the Asme*, *139*(4), 041008.

Chesnakas, C. J., & Jessup, S. D. (2003). Tip-vortex induced cavitation on a ducted propulsor. In *Proceedings of the ASME/JSME 2003 4th joint fluids summer engineering conference. Volume 1: Fora, parts A, B, C, and D. Honolulu, Hawaii, USA*

Choi, J., Oweis, G. F., & Ceccio, S. L. (2003). Vortex-vortex interactions and cavitation inception. In *Fifth international symposium on cavitation (CAV2003), Osaka, Japan.*

Doukelis, A., Mathioudakis, K., & Papailou, K. (1998). The effect of tip clearance gap size and wall rotation on the performance of a high-speed annular compressor cascade, *Proceedings of the ASME 1998 international gas turbine and aeroengine congress and exhibition. Volume 1: turbomachinery. Stockholm*.

Escudier, M. (1988). Vortex breakdown: Observations and explanations. *Progress in Aerospace Sciences*, *25*(2), 189–229.

Farrell, K. J., & Billet, M. L. (1994). A correlation of leakage vortex cavitation in axial-flow pumps. *Journal of Fluids Engineering*, *116*(3), 551–557.

Felli, M., & Falchi, M. (2011). Propeller tip and hub vortex dynamics in the interaction with a rudder. *Experiments in Fluids*, *51*, 1385–1402.

Fruman, D. H., & Aflalo, S. S. (1989). Tip vortex cavitation inhibition by drag-reducing polymer solutions. *Journal of Fluids Engineering*, *111*(2), 211–216.

Ganesh, H., Schot, J., & Ceccio, S. L. (2014). Stationary cavitation bubbles forming on a delta wing vortex. *Physics of Fluids*, *26*(12), 127102.

Gindroz, B., & Billet, M. L. (1998). Influence of the nuclei on the cavitation inception for different types of cavitation on ship propellers. *Journal of Fluids Engineering*, *120*(1), 171–178.

Gopalan, S., Katz, J., & Knio, O. (1999). The flow structure in the near field of jets and its effect on cavitation inception. *Journal of Fluid Mechanics*, *398*, 1–43.

Gopalan, S., Katz, J., & Liu, H. L.2002). Effect of gap size on tip leakage cavitation inception, associated noise and flow structure. *Journal of Fluids Engineering*, *124*(4), 994–1004.

Hall, M. G. (1972). Vortex breakdown. *Annual Review of Fluid Mechanics*, *4*(1), 195–218.

Higuchi, H., Arndt, R. E. A., & Rogers, M. F. (1989). Characteristics of tip vortex cavitation noise. *Journal of Fluids Engineering*, *111*(4), 495–501.

Hsiao, C. T., & Chahine, G. L. (2006). Effect of unsteady turbulent fluctuations on vortex/vortex/nuclei interaction. In: *26th symposium on naval hydrodynamics*.

Hsiao, C. T., & Chahine, G. L. (2008). Numerical study of cavitation inception due to vortex/Vortex interaction in a ducted propulsor. *Journal of Ship Research*, *52*(2), 114–123.

Katz, J. (1984). Cavitation phenomena within regions of flow separation. *Journal of Fluid Mechanics*, *140*, 397–436.

Katz, J., & O'Hern, T. J.1986). Cavitation in large scale shear flows. *Journal of Fluids Engineering*, *108*(3), 373–376.

Kim, J., Paterson, E. G., & Stern, F. (2006). RANS simulation of ducted marine propulsor flow including subvisual cavitation and acoustic modeling. *Journal of Fluids Engineering*, *128*(4), 799–810.

Le, T. B., Borazjani, I., Kang, S., & Sotiropoulos, F.2011, On the structure of vortex rings from inclined nozzles. *Journal of Fluid Mechanics*, *686*:451–483.

Leasca, T., Kroll, T., & Mahesh, K. (2024). Large eddy simulation of the tip leakage flow in a ducted propulsor. In *35th symposium on naval hydrodynamics*.

Li, Y., Chen, H., & Katz, J. (2017). Measurements and characterization of turbulence in the tip region of an axial compressor rotor. *Journal of Turbomachinery-Transactions of the ASME*, *139*(12), 121003.

Li, Y., Chen, H., Tan, D., & Katz, J. (2019). On the effects of tip clearance and operating condition on the flow structures within an axial turbomachine rotor passage. *Journal of Turbomachinery-Transactions of the ASME*, *141*(11), 111002.

Lim, T. T. (1998). On the breakdown of vortex rings from inclined nozzles. *Physics of Fluids*, *10*(7), 1666–1671.

Lucca-Negro, O., & O'Doherty (2001). Vortex breakdown: A review. *Progress in Energy and Combustion Science*, *27*(4), 431–481.

Michael, T., Choi, J. K., & Otero, M. (2024). Design, simulation and testing of a rotor for tip gap flow research. In *35th symposium on naval hydrodynamics*.

Ooi, K. K. (1985). Scale effects on cavitation inception in submerged water jets: A new look. *Journal of Fluid Mechanics*, *151*, 367–390.

Oweis, G. F., & Ceccio, S. L. (2005). Instantaneous and time-averaged flow fields of multiple vortices in the tip region of a ducted propulsor. *Experiments in Fluids*, *38*, 615–636.

Oweis, G. F., Fry, D., Chesnakas, C. J., Jessup, S. D., & Ceccio, S. L. (2006). Development of a tip-leakage flow part 2: Comparison between the ducted and un-ducted rotor. *Journal of Fluids Engineering*, *128*(4), 765–773.

Park, S.-I., Lee, S.-J., You, G.-S., & Suh, J.-C. (2014). An experimental study on tip vortex cavitation suppression in a marine propeller. *Journal of Ship Research*, *58*, 157–167.

Patil, K. R., Tripathi, A. D., Pathak, G., & Katti, S. S. (1991). Thermodynamic properties of aqueous electrolyte solutions. 2. Vapor pressure of aqueous solutions of sodium bromide, sodium iodide, potassium chloride, potassium bromide, potassium iodide, rubidium chloride, cesium chloride, cesium bromide, cesium iodide, magnesium chloride, calcium chloride, calcium bromide, calcium iodide, strontium chloride, strontium bromide, strontium iodide, barium chloride, and barium bromide. *Journal of Chemical and Engineering Data*, *36*(2), 225–230.

Rajagopalan, R., & Zhaoxing, Z. 1989). Performance and flow field of a ducted propeller. In *25th joint propulsion conference*.

Ran, B., & Katz, J. (1994). Pressure fluctuations and their effect on cavitation inception within water jets. *Journal of Fluid Mechanics*, *262*, 223–263.

Roth, G. I., & Katz, J. (2001). Five techniques for increasing the speed and accuracy of PIV interrogation. *Measurement Science & Technology*, *12*(3), 238–245.

Russell, P. S., Barbaca, L., Venning, J. A., Pearce, B. W., & Brandner, P. A. (2023). Influence of nucleation on cavitation inception in tip leakage flows. *Physics of Fluids*, *35*(1), 013341.

Saraswat, A., Koley, S. S., Joly, M., & Katz, J. (2025). Evolution of flow and turbulence over the entire tip region of an axial compressor rotor. *Experiments in Fluids*, *66*, 87.

Saraswat, A., Panigrahi, C., & Katz, J. (2024). Experimental characterization of the evolution of flow and turbulence in the tip region of a ducted marine propeller. In *35th Symposium on Naval Hydrodynamics*.

Sharma, S. D., Mani, K., & Arakeri, V. H.1990). Cavitation noise studies on marine propellers. *Journal of Sound and Vibration*, *138*(2), 255–283.

Stinebring, D. R., Farrell, K. J., & Billet, M. L. (1991). The structure of a three-dimensional tip vortex at high reynolds numbers. *Journal of Fluids Engineering*, *113*(3), 496–503.

Thurston, S., & Amsler, R. C. (1966). Review of marine propellers and ducted propeller propulsive devices. *Journal of Aircraft*, *3*(3), 255–261.

Thurston, S., & Evanbar, M. S. (1968). Ducted propellers for high-speed underwater propulsion. *Journal of Hydronautics*, *2*(3), 145–151.

Wang, Y., & Devenport, W. J. (2004). Wake of a compressor cascade with tip gap, part 2: Effects of endwall motion. *Aiaa Journal*, *42*(11), 2332–2340.

Wieneke, B. (2005). Stereo-PIV using self-calibration on particle images. *Experiments in Fluids*, *39*, 267–280.

Wu, H., Miorini, R. L., & Katz, J. (2011a). Measurements of the tip leakage vortex structures and turbulence in the meridional plane of an axial water-jet pump. *Experiments in Fluids*, *50*, 989–1003.

Wu, H., Miorini, R. L., Tan, D., & Katz, J. (2012). Turbulence within the tip-leakage vortex of an axial waterjet pump. *Aiaa Journal*, *50*(11), 2574–2587.

Wu, H., Tan, D., Miorini, R. L., & Katz, J. (2011b). Three-dimensional flow structures and associated turbulence in the tip region of a waterjet pump rotor blade. *Experiments in Fluids*, *51*, 1721–1737.

Wu, J., Deijlen, L., Bhatt, A., Ganesh, H., & Ceccio, S. L. (2021). Cavitation dynamics and vortex shedding in the wake of a bluff body. *Journal of Fluid Mechanics*, *917*, A26.

Cite this article: Saraswat A, Panigrahi C, Singh K and Katz J (2025). Tip leakage flow structure and cavitation inception in a ducted marine propeller. *Flow*, *5*, E35. https://doi.org/10.1017/flo.2025.10026